AIP Advances

Direct numerical simulation of a supersonic turbulent boundary layer subject to adverse pressure gradient induced by external successive compression waves

Cite as: AIP Advances 9, 085215 (2019); https://doi.org/10.1063/1.5112040
Submitted: 01 June 2019 . Accepted: 08 August 2019 . Published Online: 19 August 2019

Xu Wang, Zhenguo Wang, Mingbo Sun, Qiancheng Wang, and Zhiwei Hu

Direct numerical simulation of a supersonic turbulent boundary layer subject to adverse pressure gradient induced by external successive compression waves

Cite as: AIP Advances 9, 085215 (2019); doi: 10.1063/1.5112040
Submitted: 1 June 2019 • Accepted: 8 August 2019 •
Published Online: 19 August 2019

View Online Export Citation CrossMark

Xu Wang,[1] Zhenguo Wang,[1] Mingbo Sun,[1,a)] Qiancheng Wang,[1] and Zhiwei Hu[2]

AFFILIATIONS

[1]Science and Technology on Scramjet Laboratory, College of Aerospace Science and Engineering, National University of Defense Technology, Changsha 410073, China
[2]Aerodynamics and Flight Mechanics, Faculty of Engineering and the Environment, University of Southampton, Southampton SO17 1BJ, UK

[a)]Author to whom correspondence should be addressed: sunmingbo@nudt.edu.cn

ABSTRACT

A freestream Mach 2.9 flat-plate supersonic turbulent boundary layer subject to a "pure" adverse pressure gradient (APG) without the impact of wall curvatures is studied by direct numerical simulation and compared with a benchmark flow with zero pressure gradient. Due to APG, the streamwise velocity shows an increase in the near-wall region and a reduction in the outer boundary layer. The principal strain rate shows a sandwich distribution along the wall-normal direction. The mismatch between the temperature and velocity fluctuations in both the inner and the outer layer is observed. Enhanced LSMs (large-scale motions) and large velocity patches are the typical flow structures in the outer and inner boundary layer subject to APG, respectively. From the analysis of quadrant decomposition, the sweep events dominate in the near-wall region while ejection events dominate the rest of the boundary layer. It is found that the baroclinicity plays a significant role in the formation of the enhanced LSMs in the outer boundary layer and the near-wall velocity patches. The resulting amplified vorticity further drives the interactive motions of the outer fluid and inner fluid. The turbulent kinetic energy and turbulent Mach number profiles are amplified by APG and a second peak is observed in both profiles. Turbulent energy budget analysis demonstrates that both the production and viscous effects are strengthened in the near-wall region while in the outer layer, the production is significantly amplified and balanced by the increased convection and turbulent transport.

I. INTRODUCTION

Among internal and external flows, adverse pressure gradient (APG) is ubiquitous when interference, such as compression/shock waves, geometric curvatures are confronted. Understanding the physics of the supersonic turbulent boundary layer subject to an APG is of great value to practical engineering applications including the turbomachinery or high-speed aircrafts. APG has a tendency to destabilize the turbulent boundary layer while favorable pressure gradient (FPG) has the opposite effect to stabilize the turbulent boundary layer. For laminar boundary layer flows, APG can dramatically promote the growth of instability and accelerate flow transition.[1,2] When the APG is strong enough, a flow separation would occur in the boundary layer.[3–5]

Pressure gradients are usually characterized by the Clauser pressure gradient parameter[6] $\beta = (dp/dx)/(\tau_w/\delta^*)$ (where δ^* is the displacement thickness; τ_w is the wall shear stress; dp/dx is the streamwise pressure gradient). A positive β denotes APG while a negative value denotes FPG. In particular, $\beta = 0$ represents zero pressure gradient (ZPG). It is found that the bulk compression

$(-\nabla \cdot U)$ as well as the lateral divergence can both decrease the spanwise cross-sectional area of a fluid element which would increase the spanwise vorticity due to the angular momentum conservation. The former effect caused by the "extra strain rate" would reduce the boundary layer thickness, the latter may result in a significant impact on boundary layer properties even at a small level.[7–9] Under APG, the skin friction coefficient decreases for incompressible flows,[6,10–14] However, increases for compressible flows,[15–17] compared with ZPG turbulent boundary layer. The mean velocity profiles can be altered by APG as well. It has been reported that APG could lead to a shift of velocity below the classical log law for incompressible boundary layers[10,12,18] with exception reported where the log law is well preserved.[19] For compressible flows under APG, a shift up of the van Driest scaled velocity profiles[20,21] as well as no shift in the log law region[22] have been both observed. In addition to the likely shift of the log law, a dip in the logarithmic region is usually found and it may result from the increased length scales of the turbulent motions within the boundary layer subject to APG.[7,22,23]

Besides the mean flow properties, high-order statistical features and flow structures also show prominent differences under APG compared with ZPG boundary layer flows. The turbulent kinetic energy and Reynolds stresses have been dramatically amplified especially in the outer layer and a second peak in the outer layer has been observed when turbulent fluctuations are scaled by wall units.[11,12,24] Large-scale motions (LSMs) have been shown more energetic and active for altering the flow patterns.[13,14,25–28] Recently, the history effects of turbulent boundary layers under constant and varying APGs at matched friction Reynolds number are studied by Bobke et al.[29] They showed that the mean velocity and Reynolds stress profiles depend on the downstream development of boundary layer flows and the APG has accumulated effects on turbulent boundary layers due to history effects. For supersonic boundary layers over a concave wall, the Görtler vortices are a significant feature in promoting turbulence.[30,31] Wang et al.[32] performed a DNS on a supersonic concave turbulent boundary layer as a supplement to the experiment[33,34] conducted previously. Results showed that the streamwise extended vortices within the hairpin packets are intensified by the Görtler instability and abundant small vortices have been generated. Ejection, sweep and spanwise events are enriched by the large-scale streamwise roll cells which are considered to be the cause of the alterations of mean flow properties and turbulent statistics. Similar results have been found by Sun et al.[35] who also pointed out that the baroclinicity-induced vorticity contributes to Görtler vortices and pressure gradient could play a significant role in generating the abundant small vortices appearing in the outer boundary layer.

Although many works have been conducted on curvature induced APG boundary layers, only a few tried to isolate APG effects on supersonic turbulent boundary layer without the impact of wall curvatures. External compression waves induced APG (β_{max} = 5.8) are exerted on a flat-plate supersonic turbulent boundary layer by Fernando and Smits[22] using a two-dimensional wave generator, results are compared with the supersonic boundary layer where a similar pressure gradient is produced by a concave wall. Both the mean flow and the turbulent intensity are shown to have been strongly affected by the pressure gradient. An increasing trend of the skin friction coefficient and a decreasing trend of the friction velocity and the boundary thickness have been observed. Similar experiments have also been conducted by Smith and Smits[36] who found that the amplification of the turbulent intensity is larger and the dip in the velocity profile is more pronounced and appears earlier for the curved wall than the flat-plate counterpart. Wang et al.[37] studied a flat-plate supersonic turbulent boundary layer with Mach number 2.95 under APG produced by a compression wave generator. Results showed that the logarithmic law has been preserved while an enhanced wake region is observed. No dip of velocity profiles occurs. The principle strain and turbulent intensity are shown to increase due to APG and new velocity modes are found to change the turbulence structures. Direct numerical simulation (DNS) is confirmed to be a powerful tool in unveiling more physical details than experiments. However, works of DNS on this kind of flows are limited. More recently, Franko and Lele[21] performed a DNS study on flat plate isothermal boundary layers initially at Mach 6 with APG imposed through the freestream boundary condition. A shift up log law is observed. It was also reported that the APG increases the linear growth rate of turbulence structures and accelerates the transition to turbulence.[21]

In order to avoid the impact of coupling the effect of wall curvatures which would further introduce strong centrifugal effect, a freestream Mach 2.9 flat-plate supersonic turbulent boundary layer subject to APG (β = 2.15) induced by an external compression wave generator is studied through DNS. Mean flow properties, statistics as well as turbulence structures are analyzed and compared with a benchmark ZPG case to further understand the physics of supersonic boundary layer subject to "pure" APG. A concise introduction of a reliable in-house DNS code is presented in Sec. II. Typical mean flow properties are shown in Sec. III A, the strong Reynolds analogy is calculated which suggests a mismatch of the temperature and velocity fluctuations in the inner and outer boundary layer subject to APG. The near-wall streak structures and LSMs as well as PDFs of instantaneous flow parameters are discussed in Sec. III B. Turbulence structures and the interactive motions between inner and outer boundary layer are found to be strengthened due to pure APG and the baroclinicity seems to be an important driven force. The TKE distributions and the quadrant decomposition shown in Sec. III C will give statistical explanations to the instantaneous phenomena. Sweep events are found to dominate in the near-wall region while ejection events dominate the rest of the boundary layer. The TKE budgets show that the turbulence transport is also altered predominantly compared to the ZPG case.

II. DIRECT NUMERICAL SIMULATION

An in-house high-order finite difference DNS code[38–40] is adopted in present work to solve the three-dimensional compressible Navier-Stokes equations directly without any models. Simulations[32,35,41–44] of several different topics on supersonic flows have been conducted using this code and shown high reliability and accuracy. In present section, only a brief description will be given on the numerical methodology of the in-house DNS code.

A. Governing equations

The non-dimensionalized conservative form of the three dimensional Navier-Stocks equations in generalized curvilinear

coordinates (ξ, η, ζ) are solved in the codes and the computational domain is defined in Cartesian coordinates (x, y, z). The governing equations are non-dimensionalized by the freestream parameters and a reference length which will be described later:

$$\frac{\partial \boldsymbol{U}}{\partial t} + \frac{\partial \boldsymbol{F}}{\partial \xi} + \frac{\partial \boldsymbol{G}}{\partial \eta} + \frac{\partial \boldsymbol{H}}{\partial \zeta} = 0. \tag{1}$$

The conservative variables and flux terms are given by

$$\boldsymbol{U} = J\begin{Bmatrix} \rho \\ \rho u \\ \rho v \\ \rho w \\ \rho e \end{Bmatrix},$$

and

$$\boldsymbol{F} = \boldsymbol{F}_c + \boldsymbol{F}_v = Jr_\xi \begin{Bmatrix} \rho u^* \\ \rho u u^* + p s_x \\ \rho v u^* + p s_y \\ \rho w u^* + p s_z \\ (\rho e + p) u^* \end{Bmatrix} - Jr_\xi \begin{Bmatrix} 0 \\ \sigma_{xx} s_x + \sigma_{xy} s_y + \sigma_{xz} s_z \\ \sigma_{yx} s_x + \sigma_{yy} s_y + \sigma_{yz} s_z \\ \sigma_{zx} s_x + \sigma_{zy} s_y + \sigma_{zz} s_z \\ \tau_x s_x + \tau_y s_y + \tau_z s_z \end{Bmatrix}, \tag{2}$$

where

$$\left.\begin{aligned} s_x = \xi_x / r_\xi,\ s_y = \xi_y / r_\xi,\ s_z = \xi_z / r_\xi, \\ r_\xi = \sqrt{\xi_x^2 + \xi_y^2 + \xi_z^2},\ u^* = u s_x + v s_y + w s_z, \\ \tau_x = \sigma_{xx} u + \sigma_{xy} v + \sigma_{xz} w - q_x, \\ \tau_y = \sigma_{yx} u + \sigma_{yy} v + \sigma_{yz} w - q_y, \\ \tau_z = \sigma_{zx} u + \sigma_{zy} v + \sigma_{zz} w - q_z. \end{aligned}\right\} \tag{3}$$

Here, $\boldsymbol{F}_c$ and $\boldsymbol{F}_v$ are convective and viscous flux components respectively. The flux terms $\boldsymbol{G}$ and $\boldsymbol{H}$ are of similar forms as $\boldsymbol{F}$. The viscous stresses and heat fluxes are given in forms below,

$$\sigma_{ij} = \frac{2\mu}{Re}\left[\frac{1}{2}\left(\frac{\partial u_i}{\partial x_j} + \frac{\partial u_j}{\partial x_i}\right) - \frac{1}{3}\frac{\partial u_k}{\partial x_k}\delta_{ij}\right], \tag{4}$$

and

$$q_j = -\frac{\mu}{(\gamma - 1) Re Pr Ma_\infty^2}\frac{\partial T}{\partial x_j}. \tag{5}$$

The ideal gas state equation is exploited as a supplement to close the Navier-Stokes equations,

$$p = \frac{\rho T}{\gamma Ma_\infty^2}. \tag{6}$$

The dynamic viscosity is obtained from Sutherland's law, given by

$$\mu(T) = T^{3/2}\frac{1 + T_s/T_\infty}{T + T_s/T_\infty}, \tag{7}$$

where $T_s = 110.4$ is the Sutherland constant for air. For both ZPG and APG cases, a constant Prandtl number $Pr = 0.72$ and the specific heat ratio $\gamma = 1.4$ are used.

B. Numerical methods

An explicit 4th-oder spatial central difference scheme is adopted to solve the non-dimensionalized governing equations for the inner spatial derivatives and a 3rd-order scheme proposed by Carpenter[45] for boundary treatment. The convective terms within the governing equations are treated using entropy splitting[38] to enhance the robustness. The 3rd-order Runge-Kutta scheme is exploited for time marching. For cases when discontinuity occurs, the total variation diminishing (TVD) combined with the artificial compression method (ACM) is used.

A proper way to generate turbulent inflow conditions is always very important for simulations of fully-developed turbulent flow, here the code provides a digital filtering method introduced by Xie and Castro[46] and modified by Touber[40] for the inflow turbulent generation. This method needs a preset mean velocity profile and root-mean-square (r.m.s) fluctuating information which can be acquired from similarity solutions of a compressible laminar boundary layer and experimental data of incompressible counterparts respectively. Although the numerical filter can adjust the length scales input to match the requirement of resolution and stability and shorten the spatial distance needed to recover small-scale motions within the flow, enough distance is nevertheless necessary to allow a fully-developed turbulent flow.[43] A detailed description about this method can be found in Touber.[40]

C. Simulation set-up

The computational domain for a flat-plate supersonic turbulent boundary layer subject to APG is configured as shown in Fig. 1.

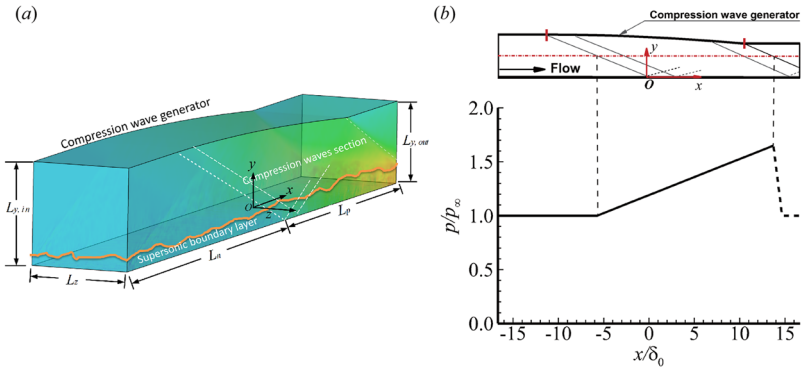

FIG. 1. (a) A sketch of the computational domain for the APG simulation. $L_{y,in}$, $L_{y,out}$ and L_z represent the inlet-section height, the outlet-section height and the width of the computational domain, respectively. The total streamwise length is separated by the coordinate origin equally. L_n and L_p represent the negative x-axis streamwise length and the positive part, respectively. (b) Illustration of the compression wave generating profile (compression wave generator) and the range of compression wave field. The pressure distribution is extracted along a line crossing the compression wave field (dash dotted line in red) from the inviscid result without reflected waves from the bottom wall. The streamwise length is normalized by nominal 99% boundary layer thickness at $x = 0$ (δ_0) and p_∞ denotes the freestream pressure.

TABLE I. Freestream conditions for both the APG simulation and the benchmark ZPG simulation.

Mach number Ma_∞	Streamwise velocity U_∞	Stagnation temperature T_0	Stagnation pressure P_0	BL 99% thickness at inlet δ_i
2.9	615 m/s	300 K	101 kPa	5.2 mm

A ZPG flat-plate supersonic turbulent boundary layer has also been simulated with same inflow conditions, domain size and grid distribution as a benchmark case for comparison. The top boundary of the APG domain contains a compression wave generating profile (compression wave generator) carefully designed using characteristics tracing technique which is in line of the experimental set-up of Wang et al.,[37] see Fig. 1(b). Fixed boundary conditions is added to the top boundary with non-zero velocity, density and temperature acquired from the characteristics tracing technique which are accordant with those of inner flow. This wall-like boundary condition can generate monotonically enhanced compression wave field (thus the increased pressure as shown in Fig. 1(b)) without introducing flow discontinuity like shock waves at supersonic inlet as non-slip wall condition would do to contaminate the wave field. When supersonic incoming freestream confronts the compression wave generating profile, successive compression waves would be generated. The incident and reflected compression waves will exert an APG on the flat-plate boundary layer over the bottom wall. The lengths of the wave generator and the top wall flat sections are so designed that it allows the reflected compression waves from the bottom wall to leave the domain without further reflection. After the compression wave generating profile, the upper boundary recover to a flat plat profile which can induce expansion waves. The domain length allows the expansion waves to escape from the outlet as well to avoid influencing the bottom wall boundary layer. The coordinate origin is set in the middle of the domain at the nominal impingement point of the first incident compression wave on the bottom wall (in fact, the first incident wave would reach slightly downstream) with x, y, z represent the streamwise, wall-normal and spanwise direction respectively. Here, we separate the computational domain as APG section (the positive-x zone) and turbulence developing section (the negative x zone). The length of the turbulence developing section is $19.2\delta_i$ (δ_i is the 99% inflow boundary layer thickness) which is long enough for the digital filtering inlet condition to develop.[40,43] Actually, previous simulations indicated that, a distance of $15\delta_i$ is considered to be suitable.[35,44]

The inflow parameters are listed in Table I which are similar to the experiments[37] and simulation[32] of Mach number $Ma = 2.95$. In the paper, subscripts "∞", "e" and "w" denotes quantities of the freestream, at the edge of the boundary layer and on the wall, respectively. The domain size and grid distributions of both the benchmark ZPG case and the APG case are displayed in Table II. δ_0 denotes the nominal 99% boundary layer thickness at $x = 0$ which is defined as the reference length. Subscripts "n" and "p" denote negative x-axis part (within the turbulence developing section) and positive part (within the APG section), respectively. The superscript "+" denotes the length scales by wall unit ν_w/u_τ. ν_w is the wall kinematic viscosity and u_τ denotes the friction velocity which is defined as $\sqrt{\tau_w/\rho_w}$, where τ_w is the wall shear stress and ρ_w the fluid density on the wall. A hyperbolic tangent stretching method[47] is adopted for grid generation in the wall-normal direction to provide better resolution in the near wall region. The distribution of grid size in the wall normal direction is given in Fig. 2. Both cases have the same grid control parameters except the refined upper zone for the compression wave generator in the APG case (not shown). Along the streamwise and spanwise directions, the grids are uniformly distributed in both cases. The resolution in wall units might differ slightly due to the change of flow properties between the ZPG and APG cases although same grid configuration is used. The grid sensitivity was tested using a grid coarsened by 50% in all directions for the APG case. Results showed that the maximum value of the skin friction coefficient varied by less than 5%. This guarantees that the grids used in present simulations are sufficiently fine to capture small-scale motions in turbulence.

TABLE II. Domain size and grid set-up for direct numerical simulations. The domain lengths are normalized by nominal 99% boundary layer thickness at $x = 0$ (δ_0). The grid spacings are normalized by the minimum wall unit in the turbulence developing section (with subscript "n") and in the APG section (with subscript "p"), respectively.

		APG case	ZPG case
Domain size	$(L_x \times (L_{y,in}; L_{y,out}) \times L_z)/\delta_0^3$	$33.3 \times (4.8; 3.8) \times 4.7$	$33.3 \times (4.8; 4.8) \times 4.7$
Grid points	$N_x \times N_y \times N_z$	$2500 \times 282^a \times 431$	$2500 \times 259 \times 431$
Grid spacing in x direction	$\Delta x_n^+; \Delta x_p^+$	4.8; 7.2	4.8; 4.8
First layer in y direction	$\Delta y_{1,n}^+; \Delta y_{1,p}^+$	0.6; 0.9	0.6; 0.6
Maximum within a δ_0	$\Delta y_{max,n}^+; \Delta y_{max,p}^+$	6.6; 9.9	6.6; 6.6
Grid spacing in z direction	$\Delta z_n^+; \Delta z_p^+$	3.9; 5.9	3.9; 3.9

[a]Extra 23 points are added to refine the upper boundary grid for the compression waves generating profile, while at the bottom wall, the first off-wall distance and grid stretching parameters are the same as the ZPG case.

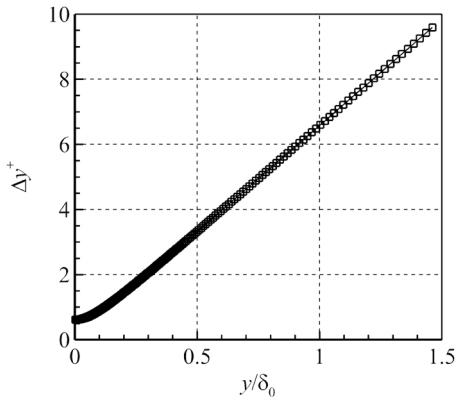

FIG. 2. The wall-normal distribution of grid spacing.

TABLE III. Mean boundary layer parameters of the benchmark ZPG simulation.

δ_0 (mm)	δ^* (mm)	θ (mm)	Re_τ	$Re_{\delta^*,vd}$	$Re_{\theta,vd}$
6.0	2.17	0.43	367.1	1750.0	1126.7

No-slip wall condition is imposed on the bottom boundary and the wall temperature is fixed to the inflow stagnation temperature (non-adiabatic wall condition). Periodic conditions are used for both spanwise boundary. Characteristic conditions[48] are applied on the top and outlet boundaries for ZPG case. Fixed top boundary with compression wave generating profile and characteristic outlet boundary are arranged for the APG case.

D. Simulation validation

The mean velocity profile and Reynolds stress are used here to validate the benchmark simulation of a ZPG supersonic turbulent boundary layer. Results of the calculated mean boundary layer parameters are given in Table III. The displacement thickness δ^* and momentum thickness θ are calculated at $x = 0$, the location the first compression wave would impinge in the ZPG case. Reynolds numbers based on the van Driest transformed displacement and momentum thicknesses $Re_{\delta^*,vd} = \rho_w U_e^{vd} \delta^{*vd}/\mu_w$, $Re_{\theta,vd} = \rho_w U_e^{vd} \theta^{vd}/\mu_w$ are also calculated as a reference for comparison with incompressible data under the hypothesis of Morkovin.[49]

Fig. 3(a) shows a comparison of the mean velocity profiles. U_{VD}^+ denotes the van Driest mean velocity scaled by the friction velocity, defined as

$$U_{VD}^+ = \frac{1}{u_\tau} \int_0^U (\overline{T}_w/\overline{T})^{1/2} dU \tag{8}$$

Results are compared in Fig. 3(a) with the incompressible DNS results of Schlatter and Örlü,[50] whose Reynolds numbers Re_τ = 359.4, Re_θ = 1006.5, and Re_{δ^*} = 1459.4 are similar with the van Driest transformed ones of the present benchmark simulation. The result from Duan et al.[52] with Ma = 2.97 and Re_τ = 486.9 is also included. The mean velocity profile agrees well with law of the wall, the logarithmic law and DNS results of Schlatter and Örlü[50] and Duan et al.[52] The log law $U_{VD}^+ = (1/\kappa)\log y^+ + C$ is plotted with κ = 0.41 and C = 5.1. The deviation occurs in wake region might be due to the non-adiabatic wall condition on the bottom domain

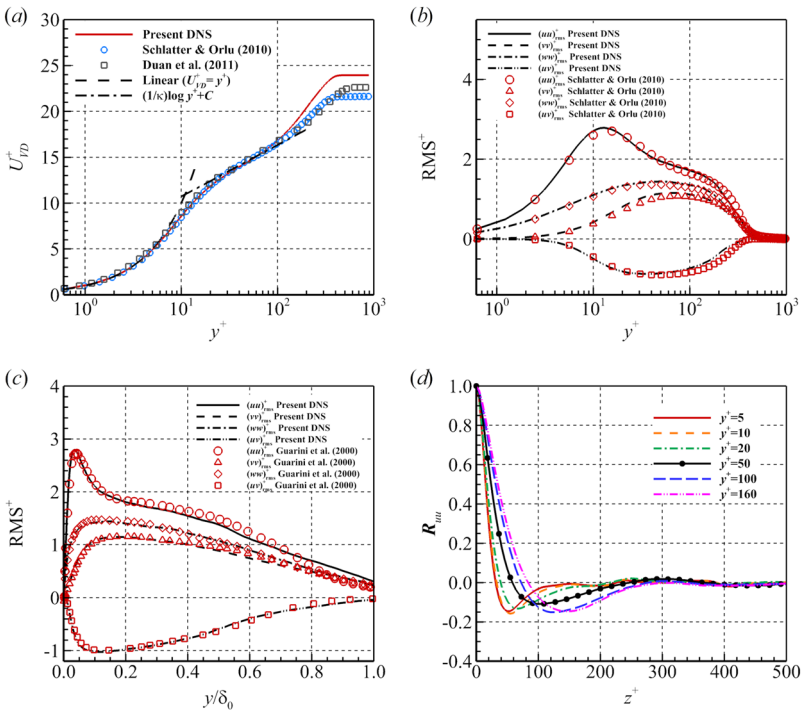

FIG. 3. Comparison of ZPG boundary layer results (at $x = 0$) with reference data: (a) mean velocity profile; (b) r.m.s velocity profiles with inner scaling compared with that of Schlatter and Örlü;[50] (c) r.m.s velocity profiles with outer scaling compared with that of Guarini et al.;[51] (d) two-point spanwise correlations of the streamwise velocity at different wall-normal positions.

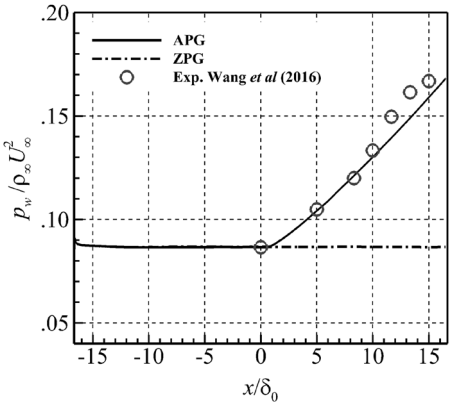

FIG. 4. Wall pressure normalized with freestream dynamic pressure.

boundary. The profiles of root-mean-square (r.m.s) velocity fluctuations together with $\overline{u'v'}$ plotted in inner and outer scaling are compared with Schlatter and Örlü[50] and Guarini et al.[51] in Fig. 3(b), (c) respectively. The r.m.s velocity components are scaled by $\sqrt{\overline{\rho}/\overline{\rho}_w}/u_\tau$, while $\overline{u'v'}$ is scaled as $(uv)^+ = \overline{\rho}_w/\overline{\rho} \cdot \overline{u'v'}/u_\tau^2$. Good agreement with references shows the reliability of the present simulation.

Two-point spanwise correlations of the streamwise velocity at different wall-normal positions of the benchmark ZPG case are given in Fig. 3(d). The spanwise separation is given in wall unit. It is clearly shown that the correlation coefficients decrease rapidly to zero well within the domain which suggesting the computational domain is sufficiently wide to allow periodic boundary condition to be applied.

Mean wall pressure of both APG and ZPG cases are illustrated in Fig. 4. The result of present APG simulation agrees well with the experimental measurements of Wang et al.[37] Within the APG section, the wall pressure grows almost linearly along the streamwise direction which confirms that the compression wave generator profile designed using the streamline tracing technique works well in generating successively enhanced compression waves field without any contamination. The non-linear distribution of the wall pressure over $10 < x/\delta_0 < 15$ in the experimental data may be resulted from the existence of weak shock waves and secondary reflection of compression waves along the rear section of compression wave generator. The Clauser pressure gradient parameter in the present simulation, $\beta = (dp/dx)/(\tau_w/\delta^*)$, is 2.15 which is similar to the experimental result of $\beta = 2.24$.[37]

III. RESULTS AND DISCUSSION

A. Mean flow and statistical properties

1. Velocity profiles

The van Driest transformed mean velocity profiles in wall units at different streamwise locations are shown in Fig. 5, along with the profile for the ZPG case at $x = 0$ for comparison. The profiles within the turbulence developing section ($x = -3\delta_0$ and $x = 0$) collapse well indicates a fully developed turbulent boundary layer has formed before the impingement of any compression wave. However, a slight difference is observed in the velocity profiles at $x = 0$ between the ZPG and APG cases. This is because the influence of compression waves which penetrate through the boundary layer slightly upstream before reaching $x = 0$ on the wall. Despite of this, the velocity profiles in the near-wall viscous sublayer ($y^+ < 6$) agree with the law of the wall well regardless of locations. The mean velocity profiles of the APG case exhibit more prominent wake regions further downstream when wall pressure rises. In the APG section (see Fig. 5(b)), the mean velocity profiles first shift above and then return back to the ZPG profile in this log law region when flow develops downstream. The shift-up trend observed within a relatively short range after the first impingement point ($x = 0$) is in accordant with the DNS result from Franko and Lele[21] which may be caused by the relaxation of β for it can not increase suddenly from zero to the expected steady value. No dip or a shift of the velocity profile below the ZPG log law has been observed. The reason for this would be related to the limited domain length. This is consistent with the experimental result of Wang et al.[37] For flat-plate boundary layers subject to APG, according to previous experiments,[22,36] the dip would only occur when the streamwise length of the APG region is sufficiently long (several times the length of present simulations).

Fig. 6 shows the mean velocity profiles in outer scaling. An obvious velocity deficit exhibits in the outer part of the boundary layer in the APG flow and a higher wall pressure leads to a larger deficit. However, from the zoomed-in view of the profiles, Fig. 6(b), an opposite trend is observed in the near-wall region, where the velocity increases with the pressure rise as the flow

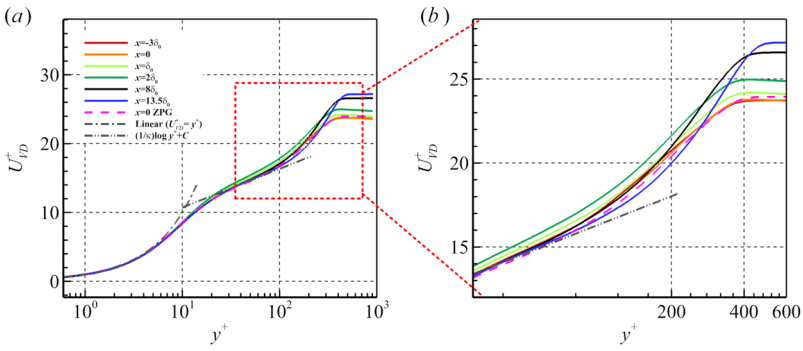

FIG. 5. (a) The mean velocity profiles normalized by wall units at different streamwise locations. (b) shows a local zoomed-in view.

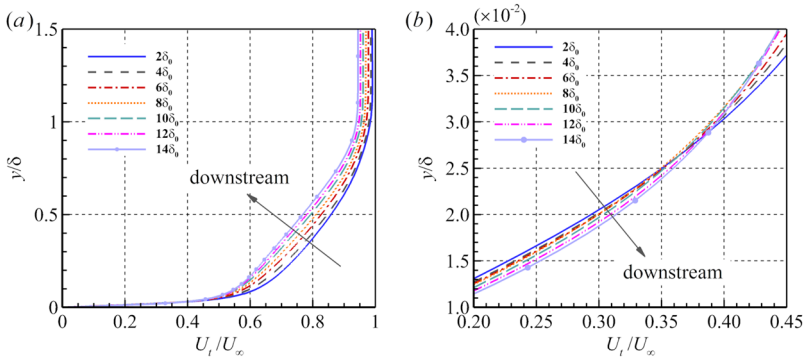

FIG. 6. (a) The mean velocity profiles scaled by the local boundary layer thickness at different streamwise locations, δ denotes the local 99% boundary layer thickness. A zoomed-in view is shown in (b) for y/δ = 0.01 to y/δ = 0.04.

develops downstream. Similar result was observed in the supersonic turbulent boundary layer over a concave wall.[32] This is related to the turbulent energy transportation influenced by compression waves and may give an explanation to the increase of wall friction which will be discussed later.

2. Skin friction

Distributions of the skin friction coefficient $C_f = \tau_w/(0.5\rho_\infty U_\infty^2)$ along the streamwise direction of both APG and ZPG cases are shown in Fig. 7(a). A slowly decreasing trend of the skin friction coefficient in the ZPG flow is observed which is consistent with the theoretical formula of Eckert[53] for turbulent boundary layer. In the turbulence developing section of APG flow, despite a slight difference within a short region before $x = 0$ which is related to the penetration of compression waves through the boundary layer as discussed earlier, the skin friction coefficient agrees well with that of the ZPG case. This shows that the flow in the turbulent developing section of the APG case is essentially the same as the ZPG case. After the turbulent developing section, the skin friction coefficient of the APG case decreases within a short distance after meeting the compression waves, then increases further downstream. The overall rising trend of the skin friction coefficient is consistent with the experimental result of Fernando and Smits[22] and is opposite to that of an incompressible boundary layer in response to an APG. The decrease of the friction velocity u_τ observed is primarily due to the increase of density at the wall (see Fig. 7(b)). The brief decrease of the skin friction coefficient immediately after $x = 0$ is likely due to the

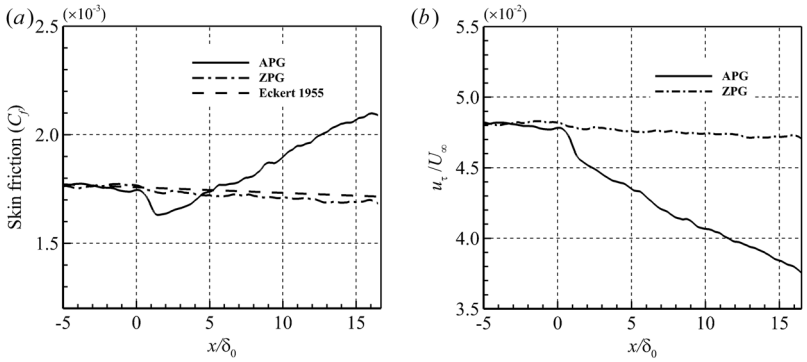

FIG. 7. The distributions of skin friction coefficient (a) and friction velocity (b) along streamwise direction.

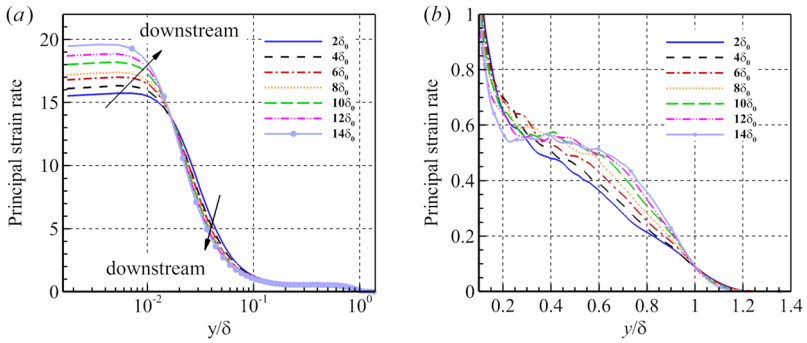

FIG. 8. The distributions of normalized principal strain rate S_u throughout local boundary layer at different streamwise locations in APG section: (a) near-wall distributions (y/δ is on log scale); (b) a local zoomed-in view from y/δ = 0.1 to y/δ = 1.4.

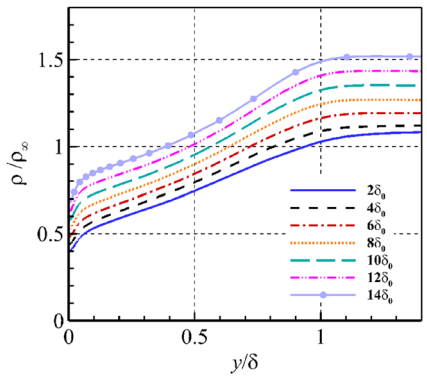

FIG. 9. The distribution of mean density throughout the boundary layer at different streamwise locations. The density is normalized by freestream density.

sudden variation of the velocity gradient imposed by the first incident compression waves. This short period of readjusting can also been seen in the friction velocity.

3. Strain rate

Fig. 8(a), (b) provide the distributions of the normalized principal strain rate S_u throughout the boundary layer at different streamwise locations in the APG section. S_u is defined as $\partial(U_t/U_\infty)/\partial(y/\delta_0)$ where U_t denotes the mean streamwise velocity. It is found that the mean shear stress in the viscous sublayer is higher than that in the logarithmic and wake regions. The principal strain rate decreases rapidly from inner to outer region of the boundary layer. Observed from Fig. 8(a), S_u has a trend of increase when pressure is enhanced in the sublayer region. However, this behavior has immediately transposed at the vicinity of $y/\delta = 0.015$ ($y^+ \approx 5$), here δ denotes the local boundary layer thickness. A second transpose of S_u, albeit not as clearly, has been found when the wall normal distance transitioning from buffer layer to logarithmic layer and wake layer (see Fig. 8(b)). Similar variation trend has been reported by Wang et al.[32] for a concave boundary layer. Combining with the mean velocity profiles given in Fig. 6, the streamwise velocity experience different increasing rates along the wall-normal direction. Under the effect of APG, the shear stress becomes higher along the flow developing direction when y/δ is approximately less than 0.015. A converse trend occurs immediately after this near-wall region until $y/\delta \approx 0.4$ ($y^+ \approx 100$). This comes up with an interesting result that the rate of velocity shows a sandwich distribution along wall-normal direction which means that the decreasing middle region is flanked by the increasing inner and outer regions. The bulk compression induced by compression waves may be the direct reason for the increased shear in the outer layer while the increase in the inner layer may result from strengthened sweep events (will be discussed later). Meanwhile, the outward motion of near-wall low-momentum fluids gives an explanation to the decrease in the middle region.

4. Thermal effects

Fig. 9 plots the mean density distributions through the boundary layer at different streamwise positions. It shows an increase of density due to the bulk compression from the induced compression waves. This leads to a decrease of the boundary thickness against the rise of wall pressure in the present simulation. The r.m.s of temperature and pressure are plotted in Fig. 10(a) (b) normalized by the local averaged temperature $<T>$ and wall dynamic pressure $\rho_w u_\tau^2$ respectively. Different trends have been observed for T_{rms} and p_{rms}. Due to the rise of pressure, the temperature fluctuation intensity increases in the inner and outer layers along the flow developing direction and decreases in the middle region ($0.03 < y/\delta < 0.4$) of the boundary layer, showing a similar variation trend with the principal strain rate. This means the thermal transport from inner to outer as well as from outer to inner boundary layer are both enhanced due to APG. It also infers an outward move of low-momentum but high-temperature fluids towards outer layer and an inward move of high-momentum but low-temperature fluids towards inner layer. In contrast to T_{rms}, the pressure fluctuation increases across the whole boundary layer as flow develops under APG, and its intensity in the inner layer is larger than that of the outer layer, this indicates a stronger volume compression of fluid in the inner layer. However, the increase rate of the pressure fluctuation shows similar trend with the r.m.s of temperature along the wall-normal direction.

The strong Reynolds analogy (SRA) is calculated and shown in Fig. 11(a) using the Morkovin relation:[49]

$$\frac{\left(\overline{T''^2}\right)^{1/2}/\tilde{T}}{(\gamma-1)Ma^2\left(\overline{u''^2}\right)^{1/2}/\tilde{u}} \approx 1, \tag{9}$$

where a tilde denotes Favre average. The results satisfy well in the mesolayer except in the inner and outer end of boundary layer. The

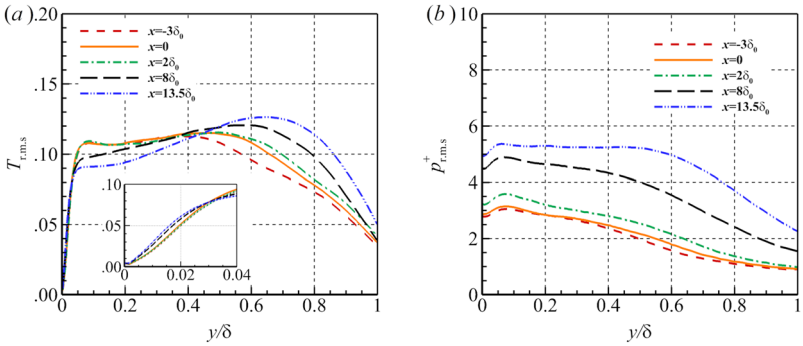

FIG. 10. The r.m.s of temperature normalized by local averaged temperature $<T>$ (a) and pressure fluctuations normalized by wall dynamic pressure $\rho_w u_\tau^2$ (b).

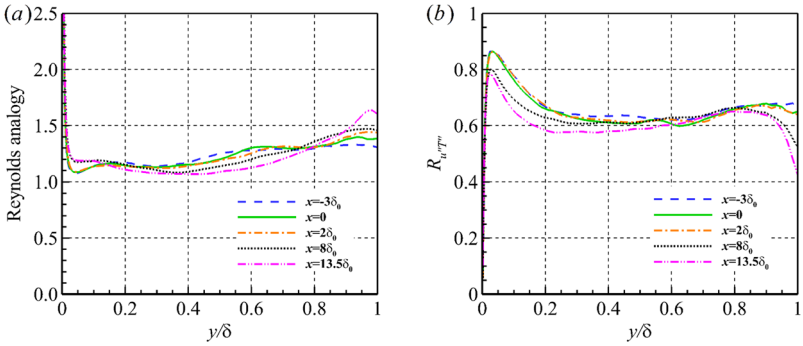

FIG. 11. The SRA (a) and $R_{u''T''}$ (b) profiles.

correlation between temperature and velocity fluctuations across the boundary layer is given by

$$R_{u''T''} = \frac{-\overline{u''T''}}{\left(\overline{u''^2}\right)^{1/2}\left(\overline{T''^2}\right)^{1/2}}. \tag{10}$$

Observed from Fig. 11(b), at all locations, the u'' and T'' are correlated albeit out of place, $R_{u''T''}$ is around 0.6 which is similar to the results of a ZPG supersonic boundary layers.[51,52] However, distinctions still exists between the inner and outer part of the boundary layer. The SRA and $R_{u''T''}$ behaviors both show a mismatch between alterations of the temperature fluctuation and the velocity fluctuation due to APG in the sublayer and wake regions indicating the effect of compressibility on the boundary layer due to APG. Similar observations have been reported for turbulent thermal boundary layers subject to adverse streamwise pressure gradients.[54] From the energy transport perspective, the results can also reflect an state of non-equilibrium of the kinetic and the internal energy. Details on turbulent energy transport will be discussed later.

B. Instantaneous flow field and turbulence structures

1. Near wall streak structures

The streamwise velocity fields at different wall-normal distances are shown in Fig. 12. Alternating low- and high-speed streaks can be clearly identified. Compared to the ZPG flow, similar near wall streaks appear in the whole turbulence developing section and only within a limited region ([0, $5\delta_0$]) in the APG section where compression waves are weak in the APG flow. When close to the wall (y/δ_0 = 0.02), we can find that within the downstream flow in the APG section, high-speed streaks are elongated and aggregates into wide patches which form a different streak pattern to the ZPG case.

At y/δ_0 = 0.25, shown in Fig. 12(b), the minimum streamwise velocity of the APG case is lower than that of the ZPG one. In the APG section, lower-momentum patches occur and have truncated and redistributed the original high-speed streaks which form the corresponding patches. The pattern given at this higher location shows the hint of the outward motion of the inner low-momentum fluid to the outer boundary layer and the interaction of outward motions and inward motions should be stronger than that in the sub-layer.

Two-point spanwise correlations of the streamwise velocity fluctuations are compared at different wall-normal distances for the APG case in Fig. 13. This can give a quantitative comparison of the spanwise space between streaks. As can be seen, at these two wall-normal locations, the streak spacing has been enlarged due to the enhanced compression waves suggesting the formation of velocity patches in the near-wall region and large-scale correlative structures in the outer layer. This trend clearly shows that

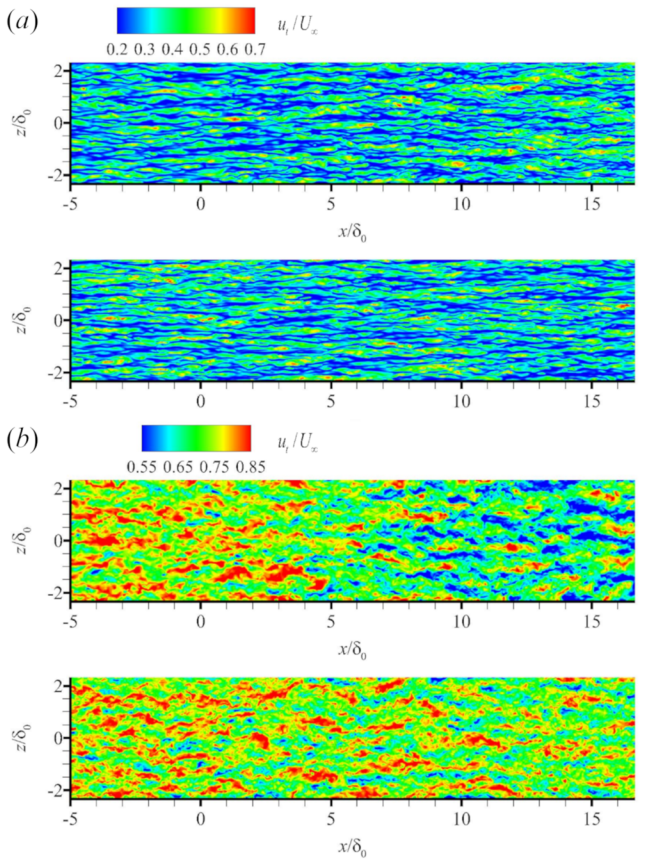

FIG. 12. Streamwise velocity contours at (a) y/δ_0 = 0.02 and (b) y/δ_0 = 0.25 within the boundary layers of the APG case (top) and the ZPG case (bottom).

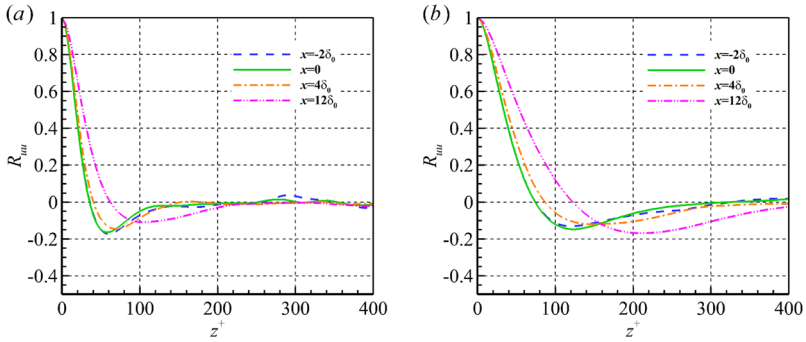

FIG. 13. Two-point spanwise correlations of streamwise velocity fluctuations at different streamwise locations in the APG case: (a) at $y/\delta_0 = 0.03$; (b) at $y/\delta_0 = 0.3$. The spanwise separation is given in wall unit.

the flow patterns in the inner and outer layers have both been greatly altered under the impact of compression waves induced by APG.

2. Large-scale motions throughout the boundary layer

Fig. 14 shows the iso-surfaces of streamwise velocity $u_t = 0.45$ for both ZPG and APG cases. It is clear that the flow pattern in the APG section has been altered due to the APG. The streamwise flow structures observed in the APG section in Fig. 14(a) organize together into large-scale patches. Some of the patches are lifted towards the outer layer while some seems to dive into the inner layer. It seems that the compression waves have enhanced the layer-to-layer interactions which have changed the corrugated flow pattern in ZPG to a rake-like pattern under the influence of APG.

To characterize vortex structures, iso-surfaces of λ_2, which is the second eigenvalue of the velocity gradient matrix[55] are plotted for the APG and the ZPG cases in Fig. 15(a) and (b), respectively. A small negative value of λ_2 (−0.06) is selected to visualize the turbulence structures and the figures are contoured by the instantaneous streamwise velocity. A wall-normal slice contour of instantaneous streamwise velocity at $y/\delta_0 = 0.5$ is also shown in the figures. Obvious differences can be observed when comparing the APG flow with the ZPG one. Attribute to bulk compression induced by compression waves the turbulence structures are "squeezed" into a thinner wall-normal zone in the APG case close to the wall. This indicates that the thickness of the boundary layer seems to become thinner due to APG which coordinates with previous studies.[22,32] When scrutinizing Fig. 15(a), apparently large vortex structures which embedded in

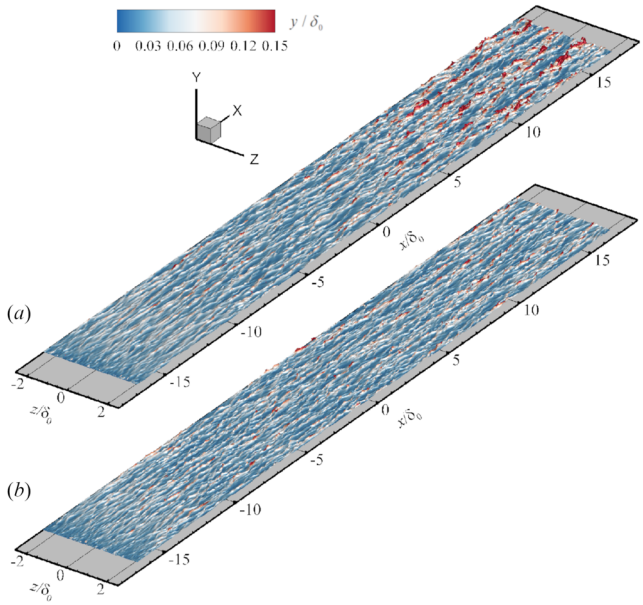

FIG. 14. Coherent structures visualized by the iso-surfaces of u_t/U_∞ colored by non-dimensional wall normal distances. (a) APG case; (b) ZPG case.

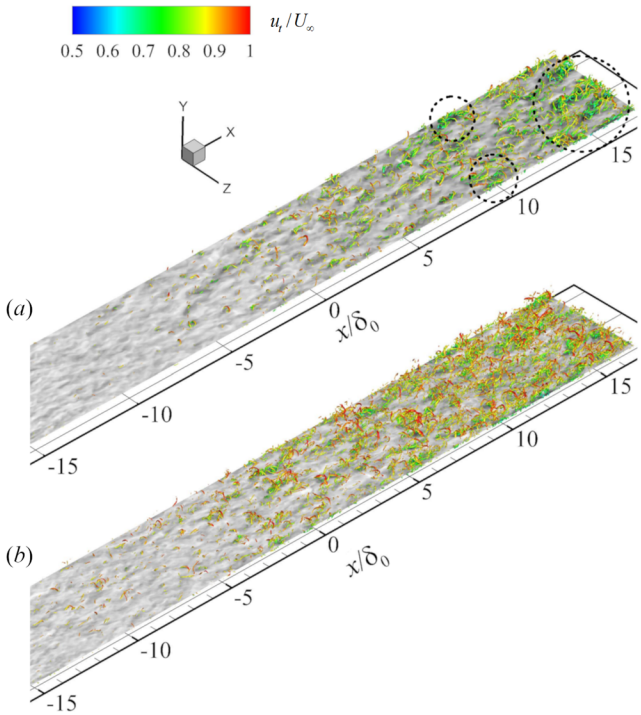

FIG. 15. The iso-surface of λ_2 colored by the non-dimensional instantaneous velocity along with a wall-normal slice contour (grayscaled) of the instantaneous streamwise velocity at $y/\delta_0 = 0.5$ ($0.5 \le u_t \le 1$, from dark to light). (a) APG case; (b) ZPG case.

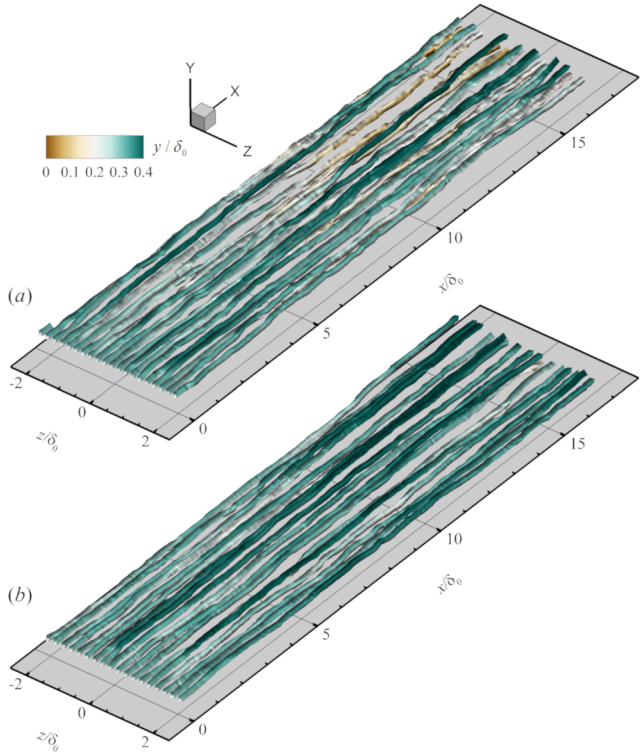

FIG. 16. Three-dimensional streamlines originated from zero-x at y/δ_0 = 0.03 colored by non-dimensional wall normal distances. (a) APG case; (b) ZPG case.

the regions of low momentum (dark regions in the grayscale slice) can be easily identified in the outer layer. Although we can also find footprints of such structures in the ZPG flow shown in Fig. 15(b), the structure scale in each direction of the APG case is obviously larger. According to previous studies[56–58] on ZPG turbulent boundary layer, these large vortical structures seem to be the LSMs where the hairpin vortices within the vortex packets align in the streamwise direction and induce regions of low streamwise momentum between their legs. These structures stretch nearly 2 ~ $3\delta_0$ in streamwise direction and about δ_0 in spanwize direction. Along with Fig. 14, the wall-normal size of these structures has been enlarged as well due to APG obviously compared with those in the ZPG case. In supersonic flows under APG effects coupling with wall curvatures, the LSMs always correlated with curvature-related Görtler-like structures,[32,35] here we find that the LSMs have been strengthened due to pure APG without effects introduced by wall curvatures.

The instantaneous streamlines, start from $x = 0$ at a wall-normal height of y/δ_0 = 0.03, are compared in Fig. 16. These streamlines are colored by the wall normal distance. The streamlines of the ZPG case are more plain without obvious deviation. However, the APG ones are more active and stratified in the wall normal direction along with the rise of compression which has the same trend as shown by the velocity iso-surfaces. The inward and outward deviations of the streamlines clearly demonstrate that the inward fluid motions from the outer layer has been dramatically enhanced and the outward motions seem to be more energetic resulting from the stronger inward motions.

To find out more details about how these enhanced LSMs are formed and their relations with the near-wall structures, contour maps of the instantaneous velocity in cross flow section at x/δ_0 = 10 are plotted in Fig. 17 to observe the flow pattern within the boundary layer. The in-plane streamtraces are also added in the figure. The general patterns of the streamwise velocity are different for the two cases. In the APG flow, the low-speed fluid close to the wall is more likely to group together and move upwards away from the wall rather than nearly uniformly distributed within the near wall region as in the ZPG flow. Higher bulge structures related to the more active upwards moving trend of the low-speed fluid are clearly observed. From the in-plane streamtraces, the large-scale paired streamwise vortices as outlined are crowd around the bulge top in the APG flow while the vortices prefer to be random and small scaled in the ZPG flow. This is consistent with the appearance of LSMs in Fig. 15. Further evidence can be found by the probability density distributions (PDF) of the streamwise vorticity along the wall normal direction at different streamwise locations shown in Fig. 18. We can clearly find that the PDFs of the streamwise vorticity collapse well in ZPG case at different wall-normal locations (see Fig. 18(b) (d)). The characteristics of self-similarity in both near-wall region and outer layer show good consistence with previous studies.[59,60] While in the near-wall region the PDF distribution is sharp and has narrow tails, in the outer layer it becomes more like Gaussian distribution and has broaden tails. This difference of PDF forms for velocity or its gradient fluctuations is always related to the level of small and large scales.[61,62] Although the symmetric feature of the PDFs in APG case remains, the self-similarity occurred in ZPG case has been violated (see Fig. 18(a) (c)). As flow develops further downstream in the APG

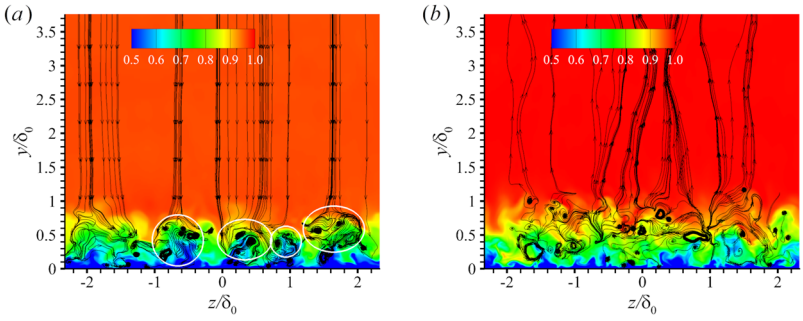

FIG. 17. Contours of streamwise velocity normalized by freestream velocity with in-plane streamlines at x/δ_0 = 10. (a) APG case; (b) ZPG case.

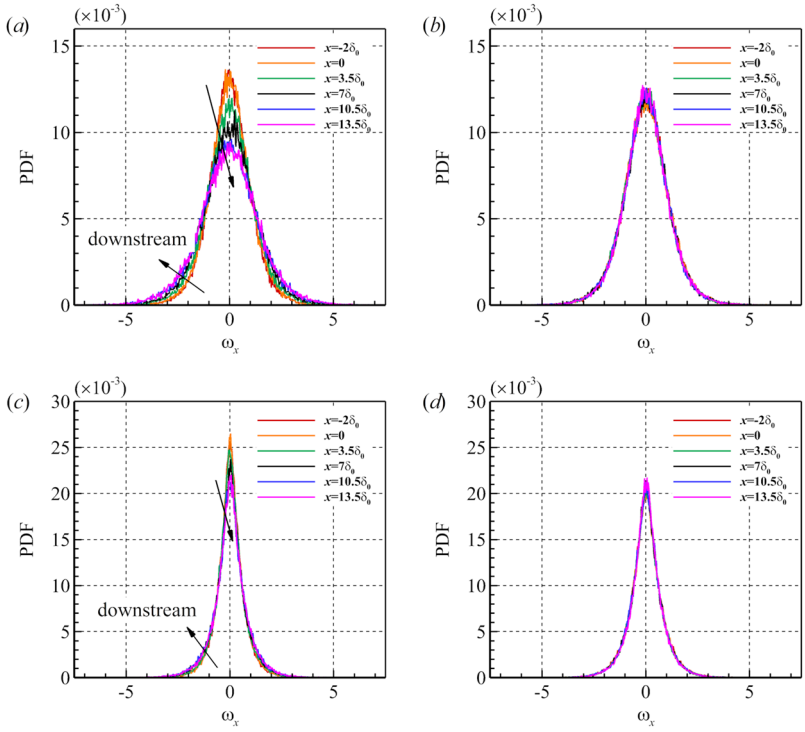

FIG. 18. The PDF of the dimensionless streamwise vorticity ω_x at different streamwise locations of the APG case (left) and the ZPG case (right): (a) (b) at y/δ_0 = 0.01; (c) (d) at y/δ_0 = 0.25.

case, the PDF shapes go less sharp and broader in both near-wall region and outer layer. This shows a clue of the scale increment and gives another evidence to the existence of strengthened vortex structures in both the outer and inner layers under the effect of APG.

To further investigate the impact of pressure gradient on vorticity, here we discuss the baroclinic term in the vorticity dynamic equation (the third term in the right hand side) which is written by

$$\frac{D\boldsymbol{\omega}}{Dt} = (\boldsymbol{\omega}\cdot\nabla)\boldsymbol{u} - \boldsymbol{\omega}(\nabla\cdot\boldsymbol{u}) - \frac{\nabla p\times\nabla\rho}{\rho^2} + \frac{\nabla p\cdot\boldsymbol{\tau}}{\rho}. \qquad (11)$$

Fig. 19 shows the contour maps of baroclinicity in a cross flow plane at x/δ_0 = 10. This term represents the cross production of the density and pressure gradients. When the local density and pressure gradients are misaligned, this term contributes to the gross vorticity increment. Carefully examination of the figure reveals that the auricle-like structures of baroclinicity are formed within the boundary layer in the APG case while no obvious alike structure is found in the ZPG one. The existence of streaks in the near wall region would induce density variation thus can increase the baroclinicity, this can be seen in the near-wall region from both cases. However, due to the pressure gradient induced by the compression waves, the additional pressure gradient has further interacted with the streak-induced density gradient which finally contributes to the vorticity increment over the wall and forms the feet of the auricle-like structures. This may give an explanation to the accumulation of low-speed fluids or patches in the near wall region of the APG flow discussed earlier. Same reasons may give to the formation of the auricle head where the LSMs may occur and interact with the compression waves which leads to larger baroclinicity than in the ZPG case. The outer-layer increased baroclinicity conversely strengthens the vorticity and further the relative motions of fluids within the boundary

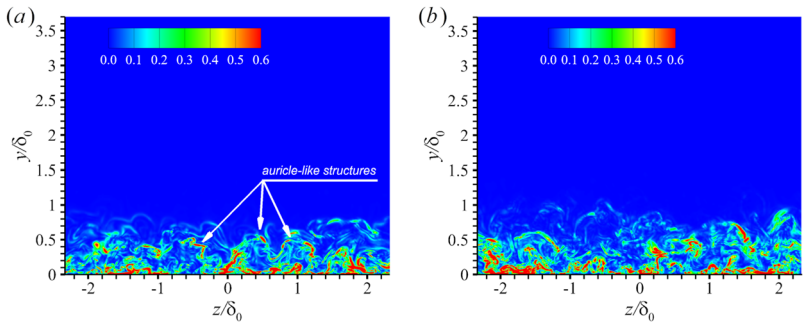

FIG. 19. Contours of the magnitude of baroclinic term ($\left|(\nabla p\times\nabla\rho)/\rho^2\right|$) normalized by freestream parameters at x/δ_0 = 10. (a) APG case; (b) ZPG case.

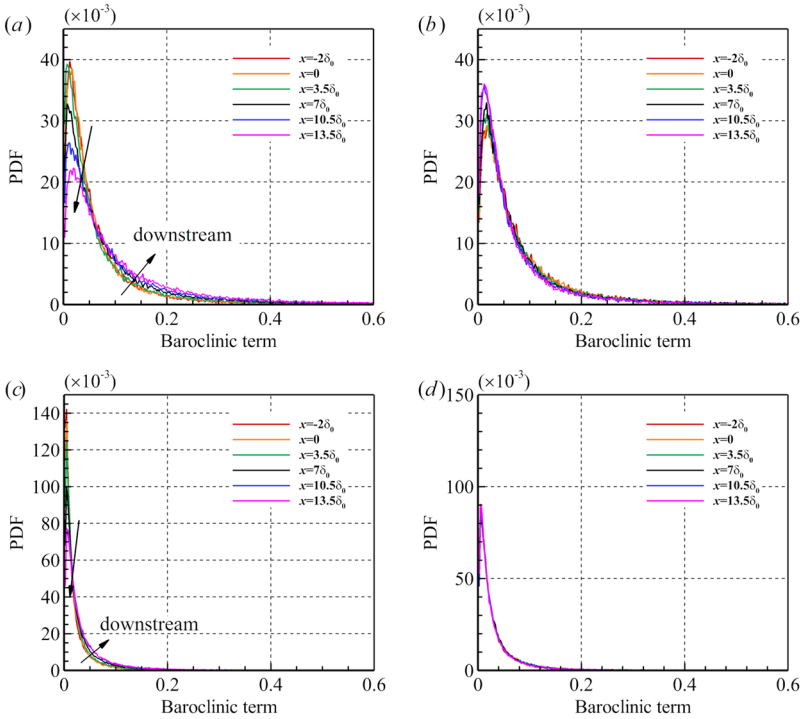

FIG. 20. The PDF of the non-dimensionlized magnitude of baroclinic term at different streamwise locations of the APG case (left) and the ZPG case (right): (a) (b) at y/δ_0 = 0.01; (c) (d) at y/δ_0 = 0.25.

layer (see in Fig. 16) resulting in the enhancement of LSMs. Eventually, the gross inward motions of high-density fluids in the outer layer (which is stronger than the outward motions caused by the reflected compression waves from the inner layer) caused by compression waves throughout the boundary layer, as can be seen in Fig. 17, form the whole auricle-like structures. The PDF of the non-dimensional baroclinic magnitude along flow developing direction at fixed wall-normal locations are given in Fig. 20. Similar distribution with that of the streamwise vorticity are shown in the figures, indicating strong correlation between the baroclinicity and vorticity generation. Hence, the large-scale streamwise vortices and the relative motions of low- and high-speed fluids within the boundary layer subject to APG could be explained by the vorticity increase due to baroclinicity. Similar conclusions have been obtained by Sun et al.[35] for a supersonic turbulent boundary layer over a concave wall. It is reported that the Görtler-like structures with the baroclinic production from the concave compression leads to the generation of abundant small-scale vortices in the outer boundary layer while the relatively slow turbulence amplification in the inner layer relies mainly on the baroclinic effect from APG.

C. Turbulent transport and TKE analysis

1. Turbulent kinetic energy distribution

The r.m.s velocity and the Reynolds stress at different streamwise locations of APG boundary layer are compared in Fig. 21–Fig. 24. Profiles of locations within the turbulence developing section ($x/\delta_0 = -3$, and $x/\delta_0 = 0$) collapse, which represents the flow has reached a state of equilibrium before entering the APG section.

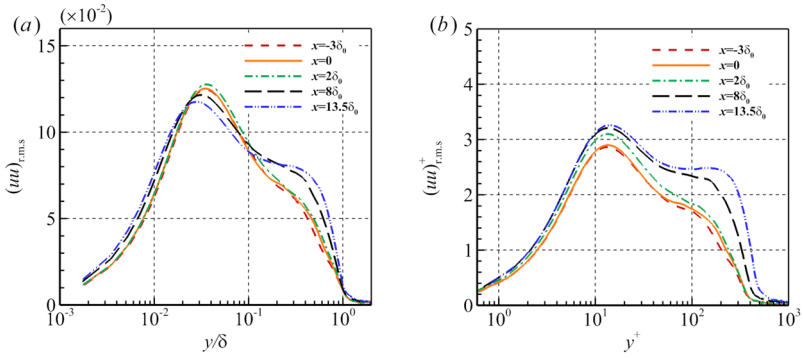

FIG. 21. The r.m.s streamwise velocity at different streamwise locations in the APG case: (a) normalized by freestream parameters; (b) normalized by wall units.

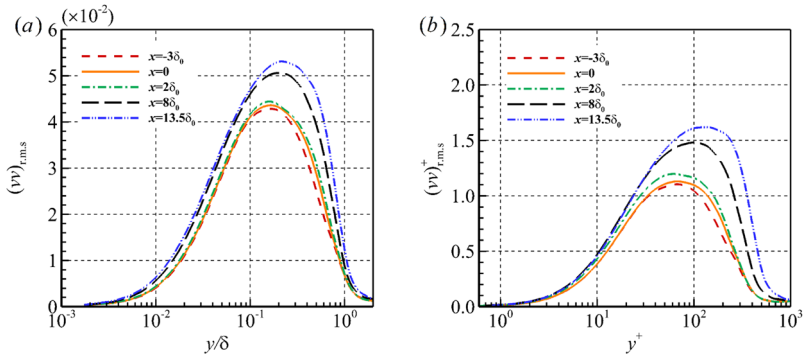

FIG. 22. The r.m.s wall-normal velocity at different streamwise locations in the APG case: (a) normalized by freestream parameters; (b) normalized by wall units.

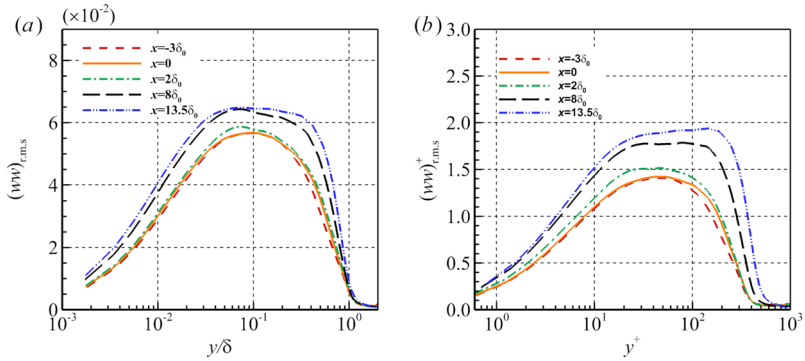

FIG. 23. The r.m.s spanwise velocity at different streamwise locations in the APG case: (a) normalized by freestream parameters; (b) normalized by wall units.

As shown in Fig. 21(a), the r.m.s streamwise velocity increases close to the wall under the APG. A peak occurs in the inner layer to a zero-pressure-gradient supersonic flow, however, the peak value has been altered by the APG. It is found that the inner-layer peak when normalized by the local freestream velocity has a trend to first increase (up to $x = 2\delta_0$) and then decrease as flow further develops downstream, this non-monotonic variation may be caused by the decrease of the local mean streamwise velocity due to the compression waves and the use of freestream bulk velocity to normalize. When the r.m.s values are scaled in wall units (Fig. 21(b)), a continued increase in the peak value is observed with the peak appearing at the same location ($y^+ \approx 15$). From both figures, a second peak can be seen in the r.m.s velocity in the outer layer and they are enhanced by the rise of pressure.

The r.m.s wall normal velocity (see Fig. 22(a) (b)) has also been amplified due to the APG. The outward move of the peak position gives a hint on the enhanced transverse motions from both the inner and outer layer which supports the discuss of instantaneous results earlier. Similar trend happens to the r.m.s spanwise velocity (see Fig. 23(a) (b)). It is interesting to note that the curve bump has been altered to become a flat due to the rise of pressure, this may support the observation on instantaneous and mean flow results of the enhanced inwards and outwards motions and the LSMs therefrom. The Reynolds stress showed in Fig. 24(a) (b) has been significantly promoted as well. The curve bump becomes sharper and has a tendency to move outwards to the outer layer, the peak position corresponds to the second peak in the streamwise velocity profile.

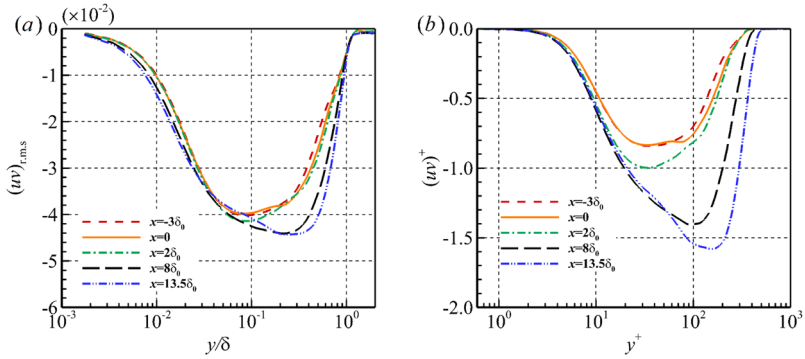

FIG. 24. The Reynolds stress distributions at different streamwise locations in the APG case: (a) normalized by freestream parameters; (b) normalized by wall units.

In a high-Reynolds-number boundary layer, the turbulent kinetic energy and Reynolds stress production can be significantly promoted in the outer layer with the contribution of outer-scaled motions.[63,64] In previous studies of the APG boundary layer, the outer peak in the turbulent intensity profiles is also reported.[12,27,32] From the above discussion of the TKE, all the profiles in the outer layer have been greatly modified due to APG. Combined with the observations of the instantaneous flow pattern, the LSMs are likely to play a key role in the process of promoting the turbulent intensity and Reynolds stress production. When carefully checking the distributions of the r.m.s velocity and Reynolds stress, the turbulent intensity within the near-wall region has also been strengthened, though not as prominently, with an increase trend when flow develops downstream. As Smits et al.[65] have pointed out that motions in the logarithmic and wake layer may have a strong influence on the behavior of the near-wall turbulence, this result gives another evidence to the instantaneous discussion of the interaction between motions from both inner and outer layers.

Turbulent Mach number $Ma_t = \sqrt{\overline{u_i'u_j'}}/\bar{c}$ (where, $\bar{c}$ denotes the local mean sonic speed) and the r.m.s of the fluctuating Mach number $Ma_{r.m.s}$ normalized by freestream parameters are also plotted at different streamwise locations in Fig. 25. Second peaks are observed in line with the turbulent kinetic energy distributions. The obvious difference between the ZPG and APG cases suggests the compressible effect play a significant role in supersonic turbulent boundary layer subject to APG.

2. Quadrant decomposition

To analyze the near-wall turbulent flow, the velocity fluctuations are categorized into four groups or quadrants within $u' - v'$ (the streamwise and wall-normal fluctuation velocities) plane using the quadrant decomposition technique.[32,66,67] Each sample of the fluctuation is regarded as an event and the events are named as outward interaction (in 1st quadrant, noted as Q1 event), ejection (Q2 event), inward interaction (Q3 event) and sweep (Q4 event), respectively.

The PDFs of $u'v'$ events at different streamwise and wall-normal locations are shown in Fig. 26. For the turbulent flow events, it is found that in the sublayer, shown in Fig. 26(a) at $y/\delta_0 = 0.01$ ($y^+ = 3$), the turbulent events are mostly with small fluctuations, especially v', giving a picture of slightly Q4 dominant at this height of the boundary layer. However, when it comes to the buffer and logarithmic layers (Fig. 26(b), (c)), fluctuation events especially the Q2 and Q4 events increase dramatically. With the rise of pressure as the flow develops downstream under APG, the events start to scatter among a relatively large area and diverge from the origin point ($u' = 0$ and $v' = 0$). Different phenomena observed in the ZPG flow where all the events gathered within a smaller area and converge around the origin point. This gives a direct sense that the ejection and sweep events are strengthened due to the APG. Both Q2 and Q4 events are related to the transverse motions in the wall normal direction and the Reynolds stress. This further indicates that the inwards motions of high-speed fluids as well as the outwards motions of low-speed fluids have been significantly strengthened by APG. The turbulent intensity is also promoted due to the responsively enhanced Reynolds stress.

The PDFs of the spanwise fluctuations are also plotted in Fig. 27 for different streamwise locations at fixed wall-normal positions ($y/\delta_0 = 0.01$ and $y/\delta_0 = 0.2$) for both the APG and ZPG cases. Similar distributions with that shown in Fig. 18 can be observed. At both wall-normal positions, self-similarity remains for the ZPG case and variations still occur along the downstream direction for the APG case. As discussed earlier, the broaden tails of PDF shapes mean a tendency of scale growth. The PDFs of the spanwise fluctuation shown in Fig. 27(a), (c) further come to a result that the spanwise scale of turbulence structures have been enlarged. Along with the discussion about PDFs of $u'v'$ events and the three-dimensional streamlines, it is natural to conclude that the streamwise vortex structures exist in both near-wall region and outer layer have been strengthened downstream the flow field due to APG. In fact, the PDFs of the velocity fluctuations in spanwise direction give a third-dimension information in addition to the quadrant decomposition.

The statistical distribution of events in different quadrants along with the streamwise locations are plotted in Fig. 28. Under the impact of APG, the events in all four quadrants rise obviously, the Q2 ejection and Q4 sweep events are dominant among all events. Their peak positions moves gradually towards the outer layer giving another evidence to the enhancement of turbulent intensity in the outer layer due to the APG which is consistent with the results discussed on turbulent kinetic energy distributions. In the near-wall region, the Q4 event contributes the majority of Reynolds stress, indicating the sweep events are dominant in the generation of the near-wall turbulence which is consistent with the earlier discuss.

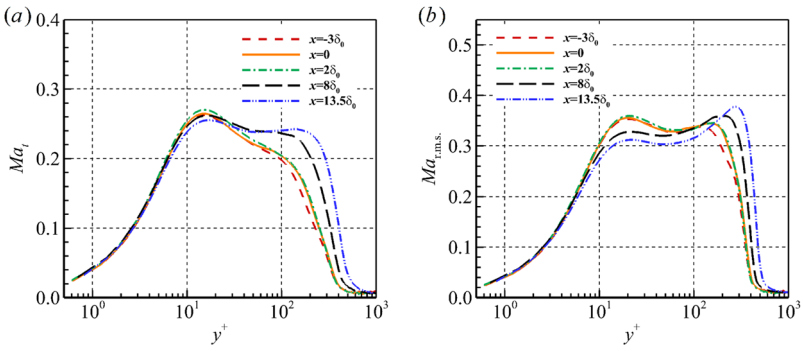

FIG. 25. The distributions of turbulent Mach number Ma_t (a) and the r.m.s of fluctuating Mach number $Ma_{r.m.s}$ (b) at different streamwise locations in APG case.

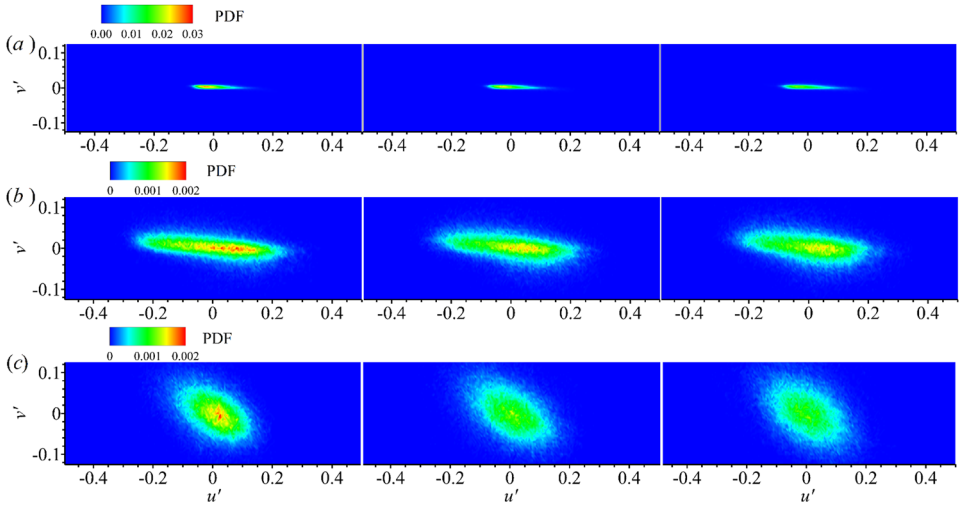

FIG. 26. The PDF of $u'v'$ events at streamwise location x/δ_0 = 0 (left), x/δ_0 = 7 (middle), x/δ_0 = 14 (right). Both u' and v' are normalized by the freestream velocity U_∞: (a) at y/δ_0 = 0.01; (b) at y/δ_0 = 0.04; (c) at y/δ_0 = 0.2 in the APG case.

The contribution of Q2 event increases faster than the Q4 event and finally dominates in the rest of the boundary layer. It is interesting that the Q2 events (solid lines) do not increase monotonically in its peak compared to the Q4 events, however the extent of Q2 events has been expended within the boundary layer. When pressure is increased, the Q4 sweep events which represent the motions from outer layer to inner layer are strengthened in response while the Q2 ejection events, which represent the motions from inner layer to outer layer, do not rely on the pressure. The large-scale vortices induced by Q4 events can also impact on the Q2 events and make them distinctive within a large extent in the boundary layer.

3. Turbulent kinetic energy budgets

The explicit form of the turbulent kinetic energy budget equation[35,51] is given by

$$\frac{\partial}{\partial t}(\bar{\rho}\bar{k}) + \tilde{u}_j \frac{\partial}{\partial x_j}(\bar{\rho}\bar{k}) = \boldsymbol{P} + \boldsymbol{T} + \boldsymbol{\Pi} + \boldsymbol{D} - \boldsymbol{\phi} + \boldsymbol{V}_c, \qquad (12)$$

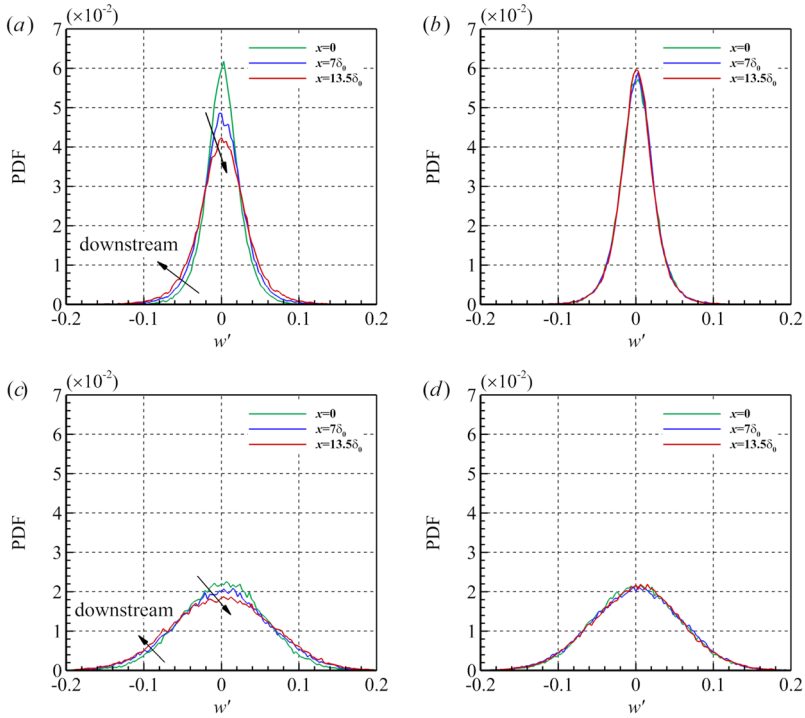

FIG. 27. The PDF of spanwise fluctuation velocity w' at different streamwise locations for fixed wall-normal positions of the APG case (left) and the ZPG case (right): (a) (b) y/δ_0 = 0.01; (c) (d) y/δ_0 = 0.2.

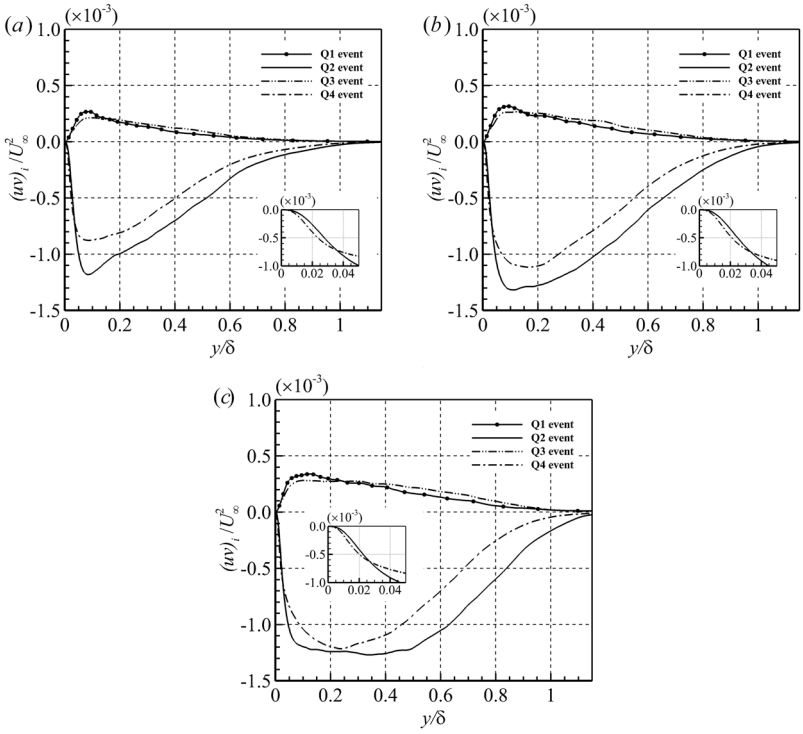

FIG. 28. The statistic distributions of quadrant decomposed Reynolds stress at different streamwise locations: (a) $x/\delta_0 = 0$; (b) $x/\delta_0 = 7$; (c) $x/\delta_0 = 14$.

where

$$\boldsymbol{P} = -\overline{\rho u_i'' u_j''}\frac{\partial \tilde{u}_i}{\partial x_j}, \tag{13}$$

$$\boldsymbol{T} = -\frac{1}{2}\frac{\partial}{\partial x_j}\overline{\rho u_i'' u_i'' u_j''}, \tag{14}$$

$$\boldsymbol{\Pi} = \boldsymbol{\Pi_t} + \boldsymbol{\Pi_d} = -\frac{\partial}{\partial x_j}\overline{p' u_i''}\delta_{ij} + \overline{p'\frac{u_i''}{x_i}}, \tag{15}$$

$$\boldsymbol{D} = -\frac{\partial}{\partial x_j}\frac{\overline{u_i''}}{Re}\tau_{ij}', \tag{16}$$

$$\phi = \overline{\frac{1}{Re}\frac{\partial u_i''}{\partial x_j}\tau_{ij}'}, \tag{17}$$

$$\boldsymbol{V_c} = -\overline{u_j''}\frac{\partial \bar{p}}{\partial x_j} + \frac{\overline{u_i''}}{Re}\frac{\partial \overline{\tau_{il}}}{\partial x_l} - \bar{\rho}\bar{k}\frac{\partial \tilde{u}_j}{\partial x_j}, \tag{18}$$

$$\boldsymbol{C} = -\tilde{u}_j\frac{\partial}{\partial x_j}(\bar{\rho}\bar{k}). \tag{19}$$

Here P represents the production term, giving the rate of generation of TKE due to velocity gradients; T the turbulent transport term; Π the combination term of pressure dilatation and diffusion; D the viscous diffusion; ϕ the viscous dissipation and C the convective term. V_c contains the terms due to the density variation, however these terms are small compared with the other terms, hence we neglect all terms in V_c here.

The energy budget at $x = 0$ in the ZPG case is plotted in Fig. 29 and is compared with the incompressible results of Schlatter and Örlü[50] at $Re_\theta = 1006$. All terms are normalized by $\rho_w u_\tau^4/\nu_w$ where ν_w denotes the kinematic viscosity at the wall region. Although slightly difference exists, which might be due to the non-adiabatic wall condition on the bottom domain boundary, the simulation result is generally consistent with the comparable results given and this confirms the reliability of present simulations and further validates the Morkovin's hypothesis.[49,68]

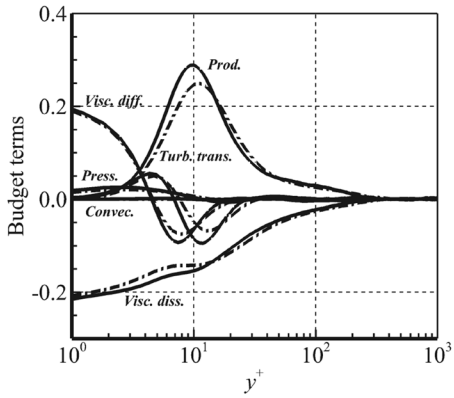

FIG. 29. The TKE budget at $x = 0$ position of the benchmark ZPG simulation (solid lines) compared with the result of incompressible case from Schlatter and Örlü[50] (dash-dotted lines).

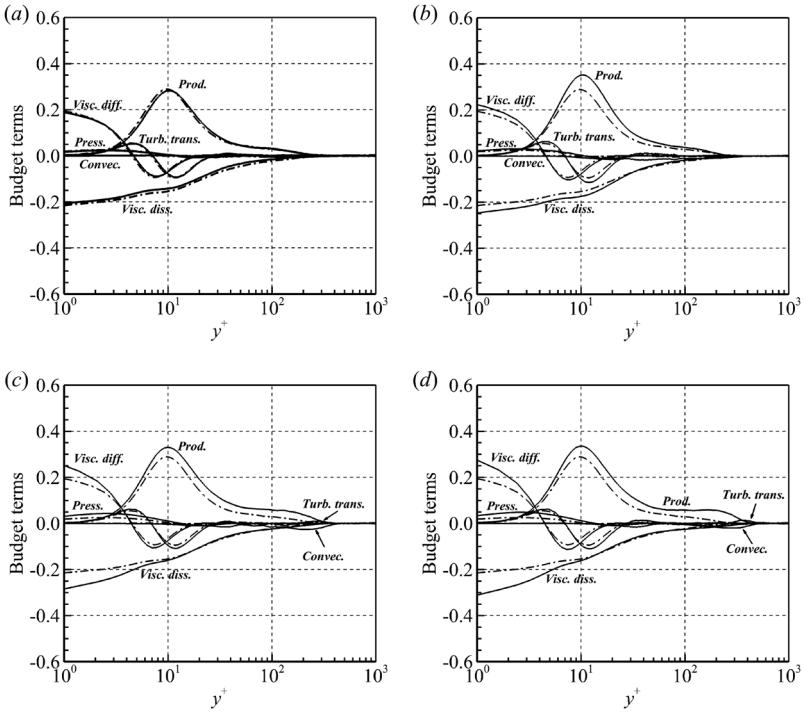

FIG. 30. The TKE budget at different streamwise locations of the APG case (solid lines) compared with the budgets of the ZPG case at corresponding locations (dash-dotted lines): (a) at $x/\delta_0 = 0$; (b) at $x/\delta_0 = 2$; (c) at $x/\delta_0 = 8$; (d) at $x/\delta_0 = 13.5$.

Fig. 30 shows the energy budget at different streamwise locations in the APG case together with the ZPG case at $x = 0$ as a reference(dash lines). The TKE budget at $x = 0$ (Figure 26(a)) in the APG flow show good agreement with that of the ZPG case. The production is balanced by the dissipation throughout the boundary layer while the viscous diffusion in the near-wall region is mainly balanced by the viscous dissipation. Similar results have been reported by Guarini et al.,[51] Pirozzoli et al[68] and Sun et al.[35]

Under the influence of APG, all terms in TKE budget are amplified, suggesting an enhancement of turbulence which is consistent with the previous discussion. In particular, the turbulent transport term increases most due to APG, meaning increase of motions between outer layer and inner layer. The augment of viscous dissipation may be caused by the increase of density due to compression waves, it can always be balanced by the increased viscous diffusion within the inner boundary. This suggests more active motions in the near wall region. In the outer layer, the production term forms a second bump in response of risen pressure suggesting a promotion of turbulent intensity within this region in the boundary layer. In accordance with the second bump in the production term, the convective term and turbulent transport term also increase prominently in the outer layer for the energy equilibrium of a new state. The strengthened balancing process in the outer layer gives another evidence on the existence of large-scale motions and their interaction with the outwards motions from inner boundary.

IV. CONCLUSIONS

A freestream Mach 2.9 flat-plate supersonic turbulent boundary layer subject to an APG ($\beta = 2.15$) is studied by DNS. The APG is carefully configured by a compression waves generator designed by characteristics tracing technique. This method can apply a "pure" APG on the flat-plate supersonic turbulent boundary layer without the impact of wall curvatures as usually do to induce pressure gradient. A ZPG flat-plate supersonic turbulent boundary layer is also simulated for validation and comparison.

The responses of the velocity profiles, skin friction as well as the principal strain rate to APG are examined. For the particular case studied with a constant $\beta = 2.15$, the logarithmic law of the velocity profile has been preserved while a more prominent wake region occurs due to APG which agrees with the experimental result of Wang et al.[37] Analyzing the local velocity profiles, the streamwise velocity shows an increase in the near-wall region and a reduction in the outer boundary layer in response to the compression waves. Increased principal strain rate is found in the near-wall and the outer boundary layer while a small region between these two regions shows a decreasing trend. Under the impact of bulk compression generated by compression waves, the density within the inner boundary layer has been promoted and in response the temperature fluctuation has been dramatically altered. The mismatch of the temperature and velocity fluctuations in the inner and outer layer is observed according to the SRA analysis and the correlation of the streamwise velocity and temperature which suggests a non-equilibrium of the velocity and the temperature fields as well as the amplified compressibility effect.

Compared with ZPG boundary layer, the near-wall streaks are more likely to group together into patches with larger spacing due to APG. Enhanced LSMs are the typical flow structures in the outer boundary layer as a consequence of the bulk compression. From the analysis of quadrant decomposition, the ejection events (Q2), sweep events (Q4) and the spanwise events are increased in the APG flow.

Results show that Q4 events dominate in the near-wall region while Q2 events dominate the rest of the boundary layer. According to a detailed analysis of the baroclinic term in the vorticity dynamic equation, it is found that the baroclinicity plays a significant role in the formation of the enhanced LSMs in the outer boundary layer and the near-wall velocity patches since the existence of the compression waves. The resulting amplified vorticity suggests to be the driven force to the inward fluid motions from the outer layer and the outward motions from the inner observed from the streamwise velocity iso-surface and the streamlines.

Both the turbulent kinetic energy and turbulent Mach number are amplified by APG and a second peak is observed in the outer region. These reflect statistically the effects of the enhanced LSMs in the APG boundary layer on the promotion of the turbulent intensity. Turbulent kinetic energy budget analysis demonstrates that both the production and viscous effects are strengthened in the near-wall region. In the outer boundary layer, the production is found to be significantly amplified and balanced by the increased convection and turbulent transport.

ACKNOWLEDGMENTS

This work was supported by National Natural Science Foundation of China (Grant No. 11522222 and 11802336). The authors would like to acknowledge Prof. Neil D. Sandham (UK) for his invaluable support and the National Supercomputer Center (Guangzhou) of China for providing high-performance computing resource used for the simulations reported in this paper.

REFERENCES

[1]K. H. Bech, D. S. Henningson, and R. A. W. M. Henkes, "Linear and nonlinear development of localized disturbances in zero and adverse pressure gradient boundary-layers," Physics of Fluids **10**, 1405–1418 (1998).
[2]M. J. P. Hack and T. A. Zaki, "Streak instabilities in boundary layers beneath free-stream turbulence," Journal of Fluid Mechanics **741**, 280–315 (2014).
[3]A. J. Smits and D. H. Wood, "The response of turbulent boundary layers to sudden perturbations," Annual Review of Fluid Mechanics **17**, 321–358 (1985).
[4]R. L. Simpson, "Turbulent boundary-layer separation," Annual Review of Fluid Mechanics **21**, 205–232 (1989).
[5]O. Lögdberg, K. Angele, and P. H. Alfredsson, "On the scaling of turbulent separating boundary layers," Physics of Fluids **20**, 075104 (2008).
[6]F. H. Clauser, "Turbulent boundary layers in adverse pressure gradients," Journal of the Aeronautical Sciences **21**, 91–108 (1954).
[7]P. Bradshaw, "The effect of mean compression or dilatation on the turbulence structure of supersonic boundary layers," Journal of Fluid Mechanics **63**, 449–464 (1974).
[8]A. J. Smits, J. A. Eaton, and P. Bradshaw, "The response of a turbulent boundary layer to lateral divergence," Journal of Fluid Mechanics **94**, 243–268 (2006).
[9]J.-H. Kim, M. Samimy, and S. Lee, "Effects of compression and expansion on turbulence intensity in supersonic boundary layers," AIAA Journal **39**, 1071–1077 (2001).
[10]P. R. Spalart and J. H. Watmuff, "Experimental and numerical study of a turbulent boundary layer with pressure gradients," Journal of Fluid Mechanics **249**, 337 (2006).
[11]J.-H. Lee and H. J. Sung, "Effects of an adverse pressure gradient on a turbulent boundary layer," International Journal of Heat and Fluid Flow **29**, 568–578 (2008).
[12]J. P. Monty, Z. Harun, and I. Marusic, "A parametric study of adverse pressure gradient turbulent boundary layers," International Journal of Heat and Fluid Flow **32**, 575–585 (2011).
[13]R. Vinuesa, R. Örlü, C. Sanmiguel Vila, A. Ianiro, S. Discetti, and P. Schlatter, "Revisiting history effects in adverse-pressure-gradient turbulent boundary layers," Flow Turbul. Combust. **99**, 565–587 (2017).
[14]R. Vinuesa, P. S. Negi, M. Atzori, A. Hanifi, D. S. Henningson, and P. Schlatter, "Turbulent boundary layers around wing sections up to Re_c=1,000,000," International Journal of Heat and Fluid Flow **72**, 86–99 (2018).
[15]W. B. Sturek and J. E. Danberg, "Supersonic turbulent boundary layer in adverse pressure gradient. Part 11: Data analysis," AIAA Journal **10**, 630–635 (1972).
[16]A. Laderman, "Adverse pressure gradient effects on supersonic boundary-layer turbulence," AIAA Journal **18**, 1186–1195 (1980).
[17]J. F. Donovan, E. F. Spina, and A. J. Smits, "The structure of a supersonic turbulent boundary layer subjected to concave surface curvature," Journal of Fluid Mechanics **259**, 1 (2006).
[18]Y. Nagano, T. Tsuji, and T. Houra, "Structure of turbulent boundary layer subjected to adverse pressure gradient," International Journal of Heat and Fluid Flow **19**, 563–572 (1998).
[19]C. D. Aubertine and J. K. Eaton, "Turbulence development in a non-equilibrium turbulent boundary layer with mild adverse pressure gradient," Journal of Fluid Mechanics **532**, 345–364 (2005).
[20]J. E. Lewis, R. L. Gran, and T. Kubota, "An experiment on the adiabatic compressible turbulent boundary layer in adverse and favourable pressure gradients," Journal of Fluid Mechanics **51**, 657–672 (2006).
[21]K. J. Franko and S. Lele, "Effect of adverse pressure gradient on high speed boundary layer transition," Physics of Fluids **26**, 024106 (2014).
[22]E. M. Fernando and A. J. Smits, "A supersonic turbulent boundary layer in an adverse pressure gradient," Journal of Fluid Mechanics **211**, 285–307 (1990).
[23]M. Jayaram, M. W. Taylor, and A. J. Smits, "The response of a compressible turbulent boundary layer to short regions of concave surface curvature," Journal of Fluid Mechanics **175**, 343 (2006).
[24]V. Kitsios, C. Atkinson, J. A. Sillero, G. Borrell, A. G. Gungor, J. Jiménez, and J. Soria, "Direct numerical simulation of a self-similar adverse pressure gradient turbulent boundary layer," International Journal of Heat and Fluid Flow **61**, 129–136 (2016).
[25]J. Lee, J. H. Lee, J.-H. Lee, and H. J. Sung, "Coherent structures in turbulent boundary layers with adverse pressure gradients," Journal of Turbulence **11**, N28 (2010).
[26]J. H. Lee, "Large-scale motions in turbulent boundary layers subjected to adverse pressure gradients," Journal of Fluid Mechanics **810**, 323–361 (2017).
[27]Z. Harun, J. P. Monty, R. Mathis, and I. Marusic, "Pressure gradient effects on the large-scale structure of turbulent boundary layers," Journal of Fluid Mechanics **715**, 477–498 (2013).
[28]Y. Maciel, A. G. Gungor, and M. Simens, "Structural differences between small and large momentum-defect turbulent boundary layers," International Journal of Heat and Fluid Flow **67**, 95–110 (2017).
[29]A. Bobke, R. Vinuesa, R. Örlü, and P. Schlatter, "History effects and near equilibrium in adverse-pressure-gradient turbulent boundary layers," Journal of Fluid Mechanics **820**, 667–692 (2017).
[30]Tandiono, S. H. Winoto, and D. A. Shah, "On the linear and nonlinear development of Görtler vortices," Physics of Fluids **20**, 094103 (2008).
[31]F. Tong, X. Li, Y. Duan, and C. Yu, "Direct numerical simulation of supersonic turbulent boundary layer subjected to a curved compression ramp," Physics of Fluids **29**, 125101 (2017).
[32]Q.-C. Wang, Z.-G. Wang, M.-B. Sun, R. Yang, Y.-X. Zhao, and Z.-W. Hu, "The amplification of large-scale motion in a supersonic concave turbulent boundary layer and its impact on the mean and statistical properties," Journal of Fluid Mechanics **863**, 454–493 (2019).
[33]Q.-C. Wang, Z.-G. Wang, and Y.-X. Zhao, "An experimental investigation of the supersonic turbulent boundary layer subjected to concave curvature," Physics of Fluids **28**, 096104 (2016).
[34]Q.-C. Wang and Z.-G. Wang, "Structural characteristics of the supersonic turbulent boundary layer subjected to concave curvature," Applied Physics Letters **108**, 114102 (2016).
[35]M. Sun, N. D. Sandham, and Z. Hu, "Turbulence structures and statistics of a supersonic turbulent boundary layer subjected to concave surface curvature," Journal of Fluid Mechanics **865**, 60–99 (2019).

[36]D. R. Smith and A. J. Smits, "A study of the effects of curvature and compression on the behavior of a supersonic turbulent boundary layer," Experiments in Fluids **18**, 363–369 (1995).
[37]Q.-C. Wang, Z.-G. Wang, and Y.-X. Zhao, "On the impact of adverse pressure gradient on the supersonic turbulent boundary layer," Physics of Fluids **28**, 116101 (2016).
[38]N. D. Sandham, Q. Li, and H. C. Yee, "Entropy splitting for high-order numerical simulation of compressible turbulence," Journal of Computational Physics **178**, 307–322 (2002).
[39]E. Touber and N. D. Sandham, "Large-eddy simulation of low-frequency unsteadiness in a turbulent shock-induced separation bubble," Theoretical and Computational Fluid Dynamics **23**, 79–107 (2009).
[40]E. Touber, "Unsteadiness in shock-wave/boundary layer interactions," Ph.d. thesis, University of Southampton (2010).
[41]N. D. Sandham, E. Schülein, A. Wagner, S. Willems, and J. Steelant, "Transitional shock-wave/boundary-layer interactions in hypersonic flow," Journal of Fluid Mechanics **752**, 349–382 (2014).
[42]N. D. Sandham, "Effects of compressibility and shock-wave interactions on turbulent shear flows," Flow, Turbulence and Combustion **97**, 1–25 (2016).
[43]B. Wang, N. D. Sandham, Z. Hu, and W. Liu, "Numerical study of oblique shock-wave/boundary-layer interaction considering sidewall effects," Journal of Fluid Mechanics **767**, 526–561 (2015).
[44]M. Sun, Z. Hu, and N. D. Sandham, "Recovery of a supersonic turbulent boundary layer after an expansion corner," Physics of Fluids **29**, 076103 (2017).
[45]M. H. Carpenter, J. Nordström, and D. Gottlieb, "A stable and conservative interface treatment of arbitrary spatial accuracy," Journal of Computational Physics **148**, 341–365 (1999).
[46]Z. Xie and I. P. Castro, "Efficient generation of inflow conditions for large-eddy simulation of street-scale flows," Flow Turbulence and Combustion **81**, 449–470 (2008).
[47]M. Vinokur, "On one-dimensional stretching functions for finite-difference calculations," Journal of Computational Physics **50**, 215–234 (1983).
[48]R. D. Sandberg and N. D. Sandham, "Nonreflecting zonal characteristic boundary condition for direct numerical simulation of aerodynamic sound," AIAA Journal **44**, 402–405 (2006).
[49]M. V. Morkovin, "Effects of compressibility on turbulent flows," Mécanique de la Turbulence **367**, 380 (1962).
[50]P. Schlatter and R. Örlü, "Assessment of direct numerical simulation data of turbulent boundary layers," Journal of Fluid Mechanics **659**, 116–126 (2010).
[51]S. E. Guarini, R. D. Moser, K. Shariff, and A. A. Wray, "Direct numerical simulation of a supersonic turbulent boundary layer at Mach 2.5," Journal of Fluid Mechanics **414**, 1–33 (2000).
[52]L. Duan, I. Beekman, and M. P. MartÍN, "Direct numerical simulation of hypersonic turbulent boundary layers. Part 3. Effect of Mach number," Journal of Fluid Mechanics **672**, 245–267 (2011).
[53]E. R. G. Eckert, "Engineering relations for friction and heat transfer to surfaces in high velocity flow," Journal of the Aeronautical Sciences **22**, 585–587 (1955).
[54]G. Araya and L. Castillo, "Direct numerical simulations of turbulent thermal boundary layers subjected to adverse streamwise pressure gradients," Physics of Fluids **25**, 095107 (2013).
[55]J. Jeong and F. Hussain, "On the identification of a vortex," Journal of Fluid Mechanics **285**, 69–94 (1995).
[56]R. J. Adrian, C. D. Meinhart, and C. D. Tomkins, "Vortex organization in the outer region of the turbulent boundary layer," Journal of Fluid Mechanics **422**, 1–54 (2000).
[57]R. J. Adrian, "Hairpin vortex organization in wall turbulence," Physics of Fluids **19**, 041301 (2007).
[58]N. Hutchins, W. T. Hambleton, and I. Marusic, "Inclined cross-stream stereo particle image velocimetry measurements in turbulent boundary layers," Journal of Fluid Mechanics **541**, 21–54 (2005).
[59]Y. Tsuji and I. Nakamura, "Probability density function in the log-law region of low Reynolds number turbulent boundary layer," Physics of Fluids **11**, 647–658 (1999).
[60]B. Lindgren, A. V. Johansson, and Y. Tsuji, "Universality of probability density distributions in the overlap region in high Reynolds number turbulent boundary layers," Physics of Fluids **16**, 2587–2591 (2004).
[61]Z. Pouransari, L. Biferale, and A. V. Johansson, "Statistical analysis of the velocity and scalar fields in reacting turbulent wall-jets," Physics of fluids **27**, 025102 (2015).
[62]A. Rasam, Z. Pouransari, L. Vervisch, and A. V. Johansson, "Assessment of subgrid-scale stress statistics in non-premixed turbulent wall-jet flames," Journal of Turbulence **17**, 471 (2016).
[63]B. Balakumar and R. Adrian, "Large- and very-large-scale motions in channel and boundary-layer flows," Philosophical Transactions of the Royal Society A: Mathematical, Physical and Engineering Sciences **365**, 665–681 (2007).
[64]N. Hutchins, T. B. Nickels, I. Marusic, and M. S. Chong, "Hot-wire spatial resolution issues in wall-bounded turbulence," Journal of Fluid Mechanics **635**, 103 (2009).
[65]A. J. Smits, B. J. Mckeon, and I. Marusic, "High-Reynolds number wall turbulence," Annual Review of Fluid Mechanics **43**, 353–375 (2011).
[66]S. S. Lu and W. W. Willmarth, "Measurements of the structure of the Reynolds stress in a turbulent boundary layer," Journal of Fluid Mechanics **60**, 481–511 (1973).
[67]N. R. Tichenor, R. A. Humble, and R. D. W. Bowersox, "Response of a hypersonic turbulent boundary layer to favourable pressure gradients," Journal of Fluid Mechanics **722**, 187–213 (2013).
[68]S. Pirozzoli, F. Grasso, and T. Gatski, "Direct numerical simulation and analysis of a spatially evolving supersonic turbulent boundary layer at M = 2.25," Physics of fluids **16**, 530–545 (2004).